A Method to Measure the Performance of Active Magnetic Regenerators

by

Aidan J. Polglase

B.Eng., University of Victoria, Canada, 2019

A Thesis Submitted in Partial Fulfillment of the Requirements for the Degree of

MASTER OF APPLIED SCIENCE

in the Department of Mechanical Engineering

A Method to Measure the Performance of Active Magnetic Regenerators

by

Aidan J. Polglase

B.Eng., University of Victoria, Canada, 2019

Supervisory Committee

_____

Dr. Andrew Rowe, Supervisor

(Department of Mechanical Engineering – University of Victoria)

_____

Dr. Rustom Bhiladvala, Departmental Member

(Department of Mechanical Engineering – University of Victoria)

ABSTRACT

Alternatives to vapour compression refrigeration cycles are needed to eliminate the use of pollution intensive refrigerants. Magnetic refrigeration (MR) exploits the magnetocaloric effect to create a refrigeration process using environmentally benign fluids and materials. Current research efforts in the field of MR focus on optimizing the active magnetic regenerator (AMR), a unique component of a magnetic refrigerator which houses the magnetocaloric material (MCM). For MR to realize its full potential as a vapour compression cycle alternative the AMR must be optimized to lower cost and improve performance. An issue in the research field of MR is the difficulty of comparing the performance of different devices in various research facilities around the globe. The standard performance metric in the field of refrigeration is the COP, which is measured on vapour compression cycles using a standard measurement procedure which is not compatible with MR devices. Additionally, the COP captures overall device performance – MR research centers around the optimization of the AMR, so a performance metric which isolates this key component and neglects inefficiencies from motors and frictional losses is more useful. Thus, the objective of this work is to define a performance metric which captures the key research targets of MR and can be compared across devices with alternate orientations, cooling capacities and AMR compositions. The COP_{AMR} performance metric has been shown to isolate the AMR in previous work, although there are challenges measuring this value on devices with a Halbach array magnetization method. This work investigates calculating the COP_{AMR} by measuring the heat rejection from the hot side heat exchanger (HEX) using a heat flux sensor (HFS). It is shown that the heat rejection from the hot HEX of a MR can be characterized as a function of device temperatures and measured heat flux from the sensor, despite the transient (oscillating) flow occurring in the HEX. By calibrating the HFS/HEX system with a resistive heating pad outputting a known heat rejection, it was possible to correlate the sensed heat to the overall heat rejection. Experiments performed on a testbench HEX device yielded relationships which can be used to calculate the total heat rejection given the sensed heat, cooling fluid temperature, and HFS temperature. Finally, the various errors of the procedures are examined, and the proposed method to retrofit MR devices with COP_{AMR} measurement capabilities is stated.

Table of Contents

List of Tables

List of Figures

ACKNOWLEDGEMENTS

I would like to thank those who I would not have been able to complete this work without:

Dr. Andrew Rowe, for your mentorship and guidance. You made it was clear from day one that my development as an engineer was the most important part of this work. Thank you for giving me the pushes I needed while letting me have the fun we all need in between.

My friends, who kept me surfing, playing music, diving, laughing and loving life throughout the past two years.

The Munchie Bar staff, for the free coffees and parking spot.

My brother, for his kindness and friendship. I am very proud of your achievements as a young engineer, but mostly just happy to have you as a brother.

My parents, for their love, encouragement and support.

Nomenclature

Abbreviations

AMR	Active magnetic regenerator
MR	Magnetic refrigeration
MCE	Magnetocaloric effect
HTF	Heat transfer fluid
MCM	Magnetocaloric material
PMMR	Permanent magnet magnetic refrigerator
PM1	Permanent magnet refrigeration prototype 1
LSR	Least squares regression
HFS	Heat Flux Sensor
HEX	Heat exchanger

Symbols

T_C	Curie temperature	K
B	Magnetic field strength	T
COP	Coefficient of performance	-
COP_{AMR}	Coefficient of performance of an active magnetic regenerator	-
R^2	Coefficient of determination	-
h_{conv}	Convection coefficient	W/m^{2}K
Nu	Nusselt number	-
k	Thermal conductivity	W/m-K
D_h	Hydraulic diameter	m
A_c	Cross sectional area	m^2
P	Perimeter	m
$\overline{T}_{C,fluid}$	Average chiller fluid temperature in hot HEX	K
$T_{C,in}$	Chiller fluid temperature at hot HEX inlet	K
$T_{C,out}$	Chiller fluid temperature at hot HEX outlet	K
$\overline{T}_{H,fluid}$	Average heat transfer fluid temperature in hot HEX	K

T_∞	Environmental temperature	K
T_{sensor}	Heat flux sensor average temperature	K
$\dot{Q}_H$	AMR heat rejection.	W
$\dot{Q}_{rejected,flow}$	The heat rejected from the hot HEX to the cooling loop.	W
$\dot{Q}_{rejected,\infty}$	The heat rejected from the hot HEX to the environment.	W
$\dot{Q}_C$	AMR cooling power.	W
$\dot{Q}_{C,input}$	Heat produced by heating pad to simulate cooling power.	W
$\dot{Q}_{C,leak}$	Heat leaking into the cold side from environment.	W
$\dot{Q}_P$	Parasitic heat leak	W
$\dot{Q}_{sensor}$	Sensed heat	W
$\dot{Q}_{bypass}$	Bypassed heat	W
R_{sensor}	Sensor thermal resistance	K/W
$R_{sensor,1}$	Sensor thermal resistance between T_{sensor} and $\bar{T}_{H,fluid}$	K/W
$R_{sensor,2}$	Sensor thermal resistance between T_{sensor} and $\bar{T}_{C,fluid}$	K/W
R_{bypass}	Bypass thermal resistance	K/W
R_{leak}	Thermal resistance to environment	K/W
$\dot{W}_{cycle}$	Cycle power	W
$\dot{W}_{pump}$	Pumping power	W
$\dot{W}_{mag}$	Magnetic power	W
V_{in}	Voltage supplied to resistive heating pad	V
I	Current supplied to resistive heating pad	A
f_s	Fraction of sensed heat	-
A_s, B_s, C_s	Sensed heat planar constants	-
A_r, B_r, C_r	Rejected heat planar constants	-
S_{total}	Total entropy	J/K
$S_{magnetic}$	Magnetic entropy	J/K
$S_{lattice}$	Lattice entropy	J/K
$S_{electronic}$	Electronic entropy	J/K

Chapter 1

Introduction

This chapter introduces the concept of magnetic refrigeration and discusses the motivation of this work, ending with a description of the structure of this thesis.

1.1 Background

In 2014 it was estimated that 7.8% of global greenhouse gas emissions (4.14 $GtCO_2eq$) could be attributed to the refrigeration sector. 63% of these emissions result from the electricity used to drive refrigeration units, while the remaining 37% result from direct emissions from chlorofluorocarbon (CFC), hydrofluorocarbon (HFC), and hydrochlorofluorocarbon (HCFC) refrigerants [1]. The Montreal Protocol implemented in 1987 quickly phased out CFCs, which rapidly destroy stratospheric ozone. HCFCs were largely used following 1987, but these refrigerants are still considered highly potent and phaseout began in 2007 and is complete in many countries. In 2016 the Kigali Amendment was added to the Montreal Protocol, which schedules an 80% reduction in HFC consumption by 2047 to help meet the goals of the Paris Agreement [2].

Alternative refrigerants with less adverse effects on greenhouse gas emissions such as natural and hydrofluoroolefin (HFO) refrigerants continue to be explored, but many of these options have various safety, cost and efficiency issues [3]. Alternatives to conventional vapour compression cycles are possible and could allow for the elimination of deleterious refrigerants.

Magnetic refrigeration (MR) employs the magnetocaloric effect (MCE) to create a refrigeration cycle using environmentally benign materials. MR was used for extremely low temperature applications (4 - 20 K) prior to 1976, when Brown [4] found that gadolinium had a strong MCE at

approximately 293 K. This discovery sparked interest in using MR for applications near room temperature. Recent research has since been aimed at optimizing MR cycles to provide competitive efficiencies, cooling capacities and costs.

1.2 Magnetocaloric Effect

The MCE is a phenomena in which the temperature of ferromagnetic materials increases when a magnetic field is applied and decreases when it is removed. Near their first and second order phase transition temperatures, certain materials exhibit more significant temperature changes than others. These materials are referred to as magnetocaloric materials (MCMs).

It is possible to express the total entropy of a magnetic material as the sum of its magnetic, electronic and lattice entropies, equation (1.1). When a magnetic field (B) is applied adiabatically the magnetic entropy ($S_{magnetic}$) decreases due to magnetic ordering. The lattice and electronic entropies ($S_{lattice}$ and $S_{electronic}$, respectively) must compensate for this change by increasing to keep constant total entropy (S_{total}), resulting in a temperature increase.

$$S_{total}(T, B) = S_{magnetic}(T, B) + S_{lattice}(T) + S_{electronic}(T) \tag{1.1}$$

The Curie temperature (T_C) is the temperature at which the MCE is maximized (usually defined by the abrupt change in heat capacity as measured in a calorimeter), and the largest temperature differential is achieved. Figure 1.1 shows an example T-S curve of a MCM near its Curie temperature before and after magnetization. The arrow represents a change in temperature due to isentropic magnetization of a MCM at its Curie temperature.
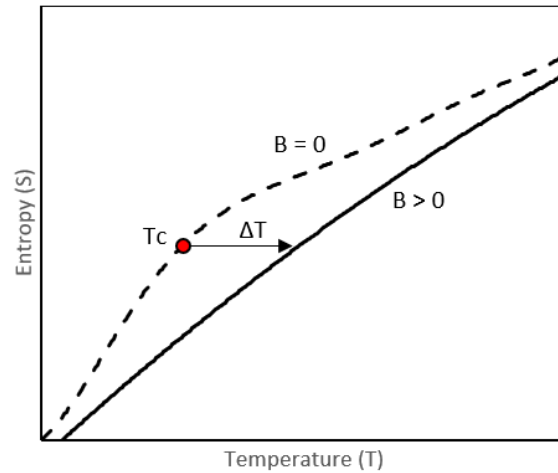
Figure 1.1: T-S diagram showing the adiabatic increase in temperature of a magnetocaloric material as the magnetic field is increased. The dashed line is the example materials T-S curve without magnetization, and the solid line represents the T-S curve after magnetization. T_C is the Curie temperature, at which the largest MCM effect (ΔT) is observed.

Now that the MCE has been introduced, the following section will discuss how this change in temperature can be harnessed in a refrigeration process.

1.3 Magnetic Refrigeration

By exploiting the MCE, it is possible to create a refrigeration process. The key component to induce MR is the active magnetic regenerator (AMR, or sometimes referred to as the regenerator): a cyclical internal flow heat exchanger which exchanges energy between a working fluid and a solid MCM matrix. AMRs are typically manufactured as tubes packed with a matrix of MCM in the form of spheres, meshes or microchannels. An optimal AMR will exhibit a large MCE and maximize heat transfer between the MCM and heat transfer fluid (HTF), while maintaining a minimal pressure drop. Carefully timed magnetization and fluid flushes through an AMR can create a significant temperature differential which can be used to pump heat. An exemplary process for a magnetic cycle is the four-step process described below. Each step outlined below is visualized in figure 1.2 with a corresponding AMR schematic showing MCM relative AMR temperature and fluid flow direction, along with a T-S diagram displaying the relative state of a MCM particle at any position x in the AMR.

A MR cycle requires the following four steps:

1. **Magnetic Heating:** The magnetic field is applied, increasing the temperature of the MCM adiabatically. See figure 1.2 showing an increase in temperature in the MCM matrix (gray box).
2. **Cold blow:** The HTF is pumped from the cold reservoir to the hot reservoir. As the fluid passes through the MCM matrix the fluid extracts heat from MCM and becomes warmer. This heat is then rejected from the hot reservoir to the environment. Figure 1.2 shows the fluid flush direction, which results in a decrease in temperature of the MCM and an increase in temperature of the pumped fluid.
3. **Magnetic cooling:** The magnetic field is removed, decreasing the temperature of the MCM adiabatically. Figure 1.2 shows a decrease in temperature in the MCM.
4. **Hot Blow:** The HTF is pumped from the hot reservoir to the cold reservoir. As the fluid loses heat to the chilled MCM and becomes cooler. This chilled fluid then extracts heat from the desired area of refrigeration. Figure 1.2 shows the fluid flush direction, which results in an increase in temperature of the MCM and a decrease in temperature of the pumped fluid.
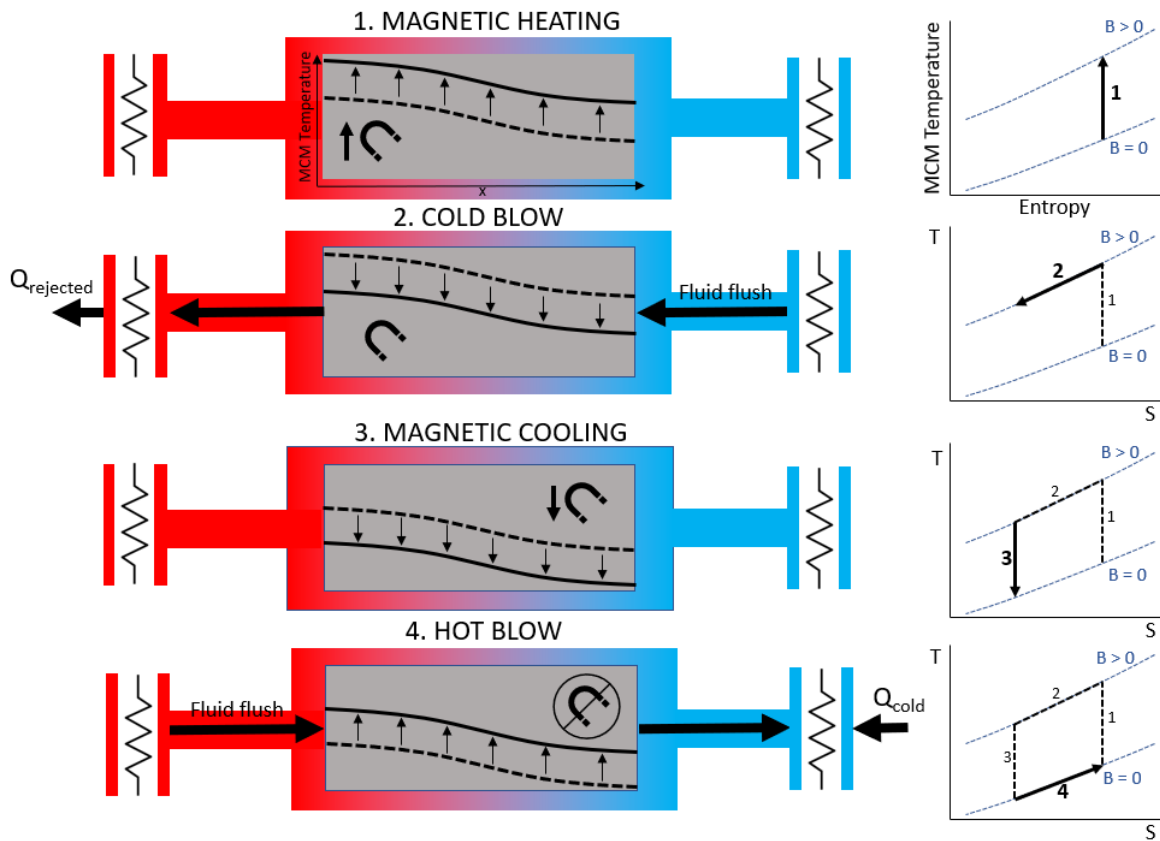
Figure 1.2: AMR diagram visualizing the four-step process (left) plus T-S diagrams showing the relative state of the MCM material at any position in the matrix (right). The grey area represents the temperature field of the MCM matrix. The AMR diagrams display the magnetization state, MCM temperature field (gray box) and fluid flow direction.

The AMR is the unique component of magnetic refrigerators, and the critical research area for the future improvement of these devices. By optimizing AMR technology in terms of cost and performance MR could become a viable heat pump method for a wide range of uses. The principal areas of research in regenerator optimization include but are not limited to:

- MCM material development (lower cost, larger MCE) [5], [6].
- AMR matrix (maximize heat transfer, minimize pressure drop).
  - Particle size and geometry.
  - Porosity/flow region [7], [8].
- Magnetic field (intensity, timing, and application method).
- Thermofluid (HTF, operating temperatures, dead volume, and utilization (Φ)).

There are many MR devices with different configurations used in research facilities around the world. Given the diversity of devices, their different strengths and weaknesses, and wide range of operating conditions, there are difficulties interpreting the performance reported in the literature. The field of MR needs a method and metric to quantify the performance of a regenerator in a MR system.

1.4 Objective

The objective of this work is to provide a method to quantify the performance of a regenerator in a MR system. This metric should capture and isolate key AMR research areas such as MCM material development, matrix geometry, magnetic field application and thermofluid properties such that a change in any property can be classified as a 'good' or 'bad' change. By quantifying AMR performance, researchers in different research facilities around the world working with devices of different layouts and sizes can more easily collaborate to advance the driving technology in the field of MR.

1.5 Thesis Structure

This thesis has been separated into 6 chapters. The document begins with an introduction to the topic of the MCE and MR, leading to the motivation for this work. The methods and procedures used and the results that followed are then presented, ending with a discussion of the key findings and some concluding thoughts. The remaining content of this thesis is as follows:

Chapter 2: Starts by discussing some of the various device layouts used in the field of MR. A metric to measure MR performance is introduced, and the theory and heat transfer characteristics of permanent magnet magnetic refrigeration (PMMR) devices are further explored.

Chapter 3: Lays out the methods used to measure the performance of a regenerator based on the theoretical findings from Chapter 2. The experimental, simulation and data analysis procedures used are then described.

Chapter 4: Presents the experimental and simulation results.

Chapter 5:   Discusses the findings of the results, as well as the potential errors of the model due to simplifications and inaccuracies.

Chapter 6:   First provides a summary of the thesis, then discusses recommendations for future work and concludes by restating the findings of this work.

Chapter 1 provided general background information, an overview of the critical research areas in magnetic refrigeration and the motivation of this work. The following chapter will further discuss the background information and theory needed to quantify the performance of a MR device.

Chapter 2

Background and Theory

This chapter begins by discussing various MR device types and mechanisms. An issue in the research and development of MR devices is the inability to collect relevant performance data that is comparable between different device layouts. This chapter examines the equations derived by Arnold et al. [9] to isolate and measure the performance of the AMR, and presents the theory needed to apply this method to cyclical permanent magnet devices.

2.1 MR Devices and Layouts

Many device layouts have been explored throughout MR research to minimize losses. One component that varies across these devices is the magnetic field application system, which has major impacts to the hydraulic, mechanical and electrical components required. The majority of recent MR research has explored the use of permanent magnet magnetic refrigeration (PMMR) systems due to the simplicity, durability and high performance [10], [11], [12], [13]. There are three orientations commonly used on PMMR devices: Halbach cylinder, reciprocating magnet, and rotating magnet [14]. Figure 2.1 below shows simplified diagrams of each PMMR method. The device shown in O1 uses two rotating concentric Halbach pairs to create a sinusoidal magnetic field waveform which is applied to an AMR located in the center of the cylinders. O2 depicts a reciprocating magnet device, which slides a permanent magnet back and forth over one or multiple AMRs. O3 shows a schematic of a rotating magnet system, which rotates a permanent magnet around an array of AMRs creating a cycle of magnetization and demagnetization. All magnetization methods are typically operated by a motor.

O1: Halbach cylinders   O2: Reciprocating magnet   O3: Rotating magnet
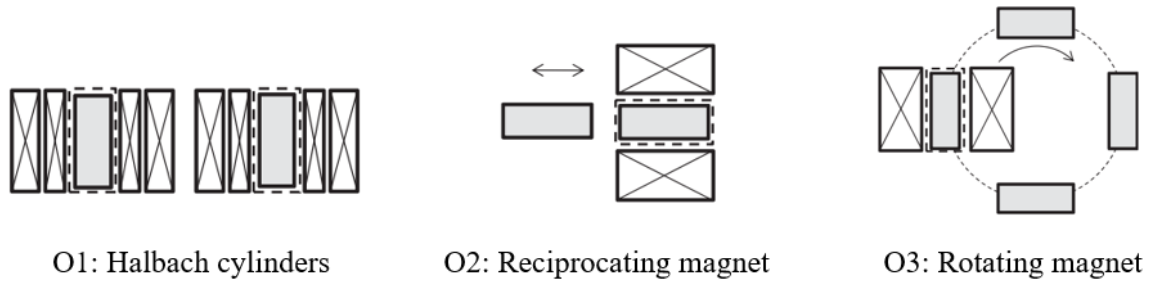
Figure 2.1: Diagrams of the three commonly used PMMR device orientations [14].

Permanent Magnet Refrigeration Prototype 1 (PM1) is a PMMR device developed at the University of Victoria in 2011 [15]. PM1 remains a valuable MR research tool due to the device's ideal combination of simplicity and performance. As shown in figure 2.2, the device uses a motor driven Halbach array to induce timed magnetization, and a hydraulic displacer to pump the HTF back and forth.
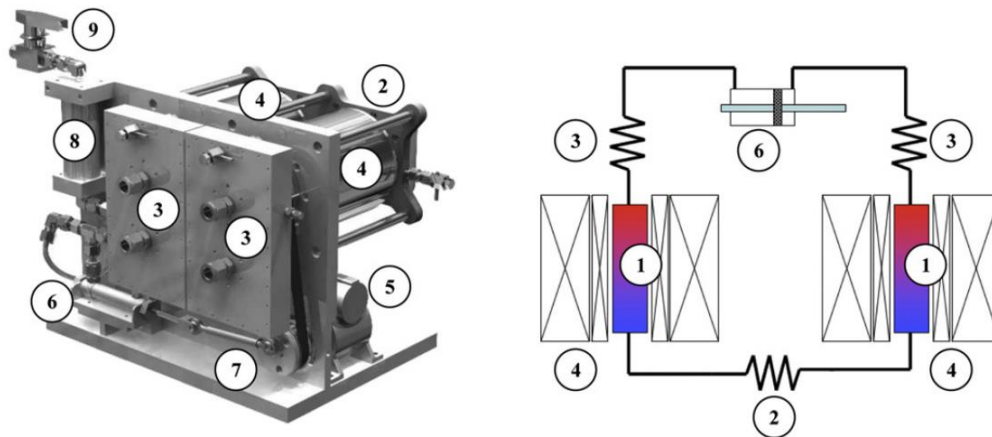
Figure 2.2: PM1 rendering (left) and schematic (right). (1) AMRs (displayed only in the schematic), (2) cold HEX, (3) hot HEX, (4) Halbach cylinders, (5) DC gearmotor, (6) Hydraulic displacer, (7) Crank mechanism, (8) Accumulator, (9) Valve [15].

PM1's control system allows the user to control the displacer frequency (f), cooling power ($\dot{Q}_{C,input}$) simulated by a resistive heating pad located in the cold HEX, and the chiller fluid temperature ($\bar{T}_{C,fluid}$). The chiller fluid is an external flow loop used to facilitate heat rejection in the hot HEX. PM1's instrumentation system allows the measurement of temperatures at various locations (Ambient, casing, and HTF at HEX inlets and outlets) and the internal pressure. PM1 does not currently have an effective method of measuring performance.

2.2 Performance

The standard metric for measuring performance in the field of refrigeration is the coefficient of performance (*COP*). The *COP* typically states the ratio of the cooling power to the total power required to run the unit. This metric is convenient for consumers as it reflects the cost to run the device. The reporting of the *COP* of refrigeration products is standardized, with set evaporator and condenser temperatures depending on the refrigerant the device uses. No *COP* standard measurement method has been developed for MR devices using various MCMs. In the field of MR, performance is often reported by the cooling power at a certain temperature span across the AMR, as demonstrated in Vieira et al. [5]. This method can show whether certain changes have a positive or negative impact on device performance. Unfortunately, this method cannot be used to compare results across other studies and MR devices because cooling power and temperature span depend heavily on device characteristics such as MCM quantity, device geometry and many other variables. Typical *COP* measurements are performed by measuring the electrical power delivered to the motor or compressor (in vapour-compression cycles). Thus, many of the losses captured by a *COP* value do not relate to the performance of the areas central to MR optimization. For example, the performance of a device with an inefficient motor but excellent MCM may appear to perform similarly to a device with a highly efficient motor but poor MCM. A method to measure the performance of an AMR isolated from the losses and efficiencies outside the main scope of MR research is needed in the field so that regenerator optimization can be researched on any device around the world.

Arnold et al. [9] proposes using the alternative *COP*$_{AMR}$ value that isolates the AMR for research purposes:

$$COP_{AMR} = \frac{\dot{Q}_C}{\dot{W}_{cycle}} \tag{2.1}$$

Where $\dot{Q}_c$ is the cooling power, or the heat extracted from the cold reservoir and passed to the AMR. $\dot{W}_{cycle}$ can be defined as:

$$\dot{W}_{cycle} = \dot{W}_{pump} + \dot{W}_{mag} \tag{2.2}$$

Where $\dot{W}_{pump}$ is the power required to pump the HTF, and $\dot{W}_{mag}$ is the power required to magnetize the MCM. Conveniently, both metrics isolate the key research areas previously noted in section 1.3 (material development, AMR matrix optimization, magnetic field application and HTF). $\dot{W}_{pump}$ is affected by the HTF properties and the AMR matrix geometry. An optimized regenerator will have a low pressure drop across the MCM matrix, and thus a lower $\dot{W}_{pump}$ requirement. The magnetic power requirement ($\dot{W}_{mag}$) can be decreased by optimizing the magnetic field application method and the MCM material. With effective magnetization and materials, a large MCE can be observed with less energy demand.

Arnold et al. uses a force transducer to measure $\dot{W}_{cycle}$ on the crank arm of a MR system with a reciprocating magnet PMMR device (O2 in figure 2.1) [9]. This method was shown to be very effective for that device; however, on systems such as PM1 which use a rotating Halbach array (O1 in figure 2.1) this method can not be used to calculate the $\dot{W}_{mag}$ term.

Thus, the focus of the research summarized by this paper is to develop and test a method to measure the COP_{AMR} of a PM system with a rotating Halbach array.

2.3 MR Heat Transfer Theory

Equation (2.1) can be better understood by examining an energy flow diagram of an MR system. Figure 2.3 shows the heat transfer that occurs between the key components of a PMMR system. Arrows represent the flow of heat and power between the AMR, hot and cold HEX, heating pad and chiller fluid.
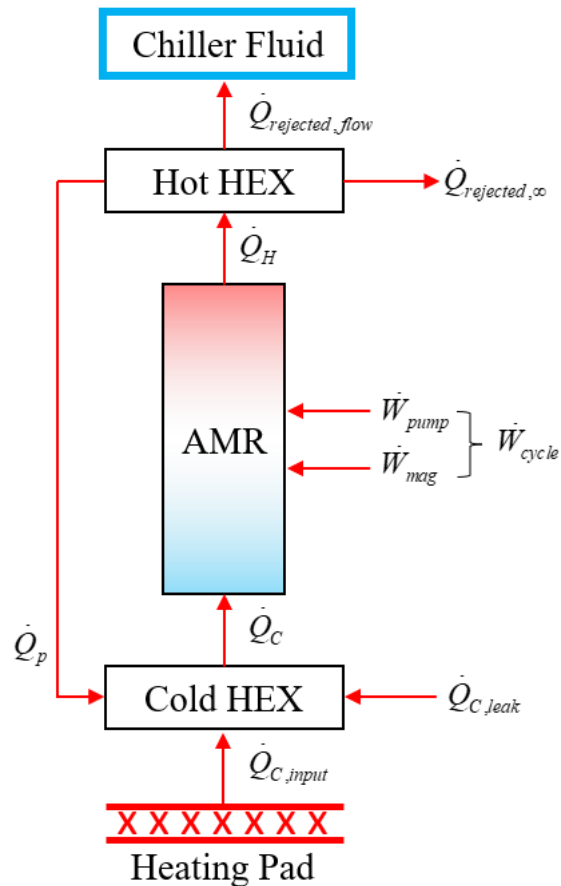
Figure 2.3: Magnetic refrigeration energy flow process diagram. Red arrows represent heat and power exchange between device components.

Several variables shown in figure 2.3 above have not been previously discussed. These variables are identified in table 2.1 below, and their relevance is discussed in the remainder of this section of the thesis.

Table 2.1: Variables relating to the energy flow of PM1 shown in figure 2.3.

Variable	Description
$\dot{Q}_{C,input}$	Heat produced by heating pad to simulate cooling power.
$\dot{Q}_{C,leak}$	Heat leaking into the cold side from environment.
$\dot{Q}_P$	Parasitic heat leak between reservoirs through the device's components.
$\dot{Q}_{rejected,flow}$	The heat rejected from the hot HEX to the cooling loop.
$\dot{Q}_{rejected,\infty}$	The heat rejected from the hot HEX to the environment.
$\dot{Q}_H$	AMR heat rejection.
$\dot{Q}_C$	AMR cooling power.

Recalling equation (2.1):

$$COP_{AMR} = \frac{\dot{Q}_c}{\dot{W}_{cycle}}$$

It should be restated that it is difficult to measure the magnetic power component of $\dot{W}_{cycle}$ on a rotary Halbach MR system, so replacing this variable with one that is easier to measure is desirable. By examining the energy flow diagram in figure 2.3 it is evident that $\dot{W}_{cycle}$ can be rewritten as:

$$\dot{W}_{cycle} = \dot{Q}_H - \dot{Q}_C \tag{2.3}$$

And therefore,

$$COP_{AMR} = \frac{\dot{Q}_C}{\dot{Q}_H - \dot{Q}_C} \tag{2.4}$$

Where,

$$\dot{Q}_C = \dot{Q}_{C,input} + \dot{Q}_{leak,C} + \dot{Q}_P \tag{2.5}$$

$$\dot{Q}_H = \dot{Q}_{rejected,flow} + \dot{Q}_{rejected,\infty} + \dot{Q}_P \tag{2.6}$$

And finally,

$$COP_{AMR} = \frac{\dot{Q}_{C,input} + \dot{Q}_{C,leak} + \dot{Q}_P}{\dot{Q}_{rejected,flow} + \dot{Q}_{rejected,\infty} - \dot{Q}_{C,input} - \dot{Q}_{C,leak}} \tag{2.7}$$

Measurement of the COP_{AMR} can be found by measuring the parameters of equation (2.7). $\dot{Q}_{C,input}$ can be measured as the electrical power supplied to the heating pad. $\dot{Q}_{C,leak}$ is linearly dependent on the insulation between the cold reservoir and the environment. The PM1 cold HEX design has significant insulation to the environment, and thus perfect environmental isolation ($\dot{Q}_{C,leak} = 0$) is assumed. On other device layouts, a simulation based linear approximation could be used to estimate this relationship. The parasitic heat loss $\dot{Q}_P$ is the heat transfer between the hot and cold reservoir through the casings of the MR device. Tura et al. [16] was able to estimate the parasitic heat loss of an MR device as a linear function of the temperature span between the hot and cold reservoir using a geometric model. The parasitic heat loss of PM1 remains unexamined, although the work done by Tura et al. shows that this approximation can be made quite easily on any MR device. This leaves the heat rejected from the hot HEX ($\dot{Q}_H$) which is composed of the heat rejected to the cooling loop ($\dot{Q}_{rejected,fluid}$) and the heat rejected to the environment ($\dot{Q}_{rejected,\infty}$).

Now that it has been shown that the COP_{AMR} can be calculated by measuring the rejected heat $\dot{Q}_H$, the scope of this work can be narrowed to determining the best method to measure the rejected heat on any PMMR device. The following section will discuss the methods used to develop a technique to measure the rejected heat, and consequentially COP_{AMR} of a PMMR device.

Chapter 3

Methods

This chapter explains and justifies the methods used in this work to measure the rejected heat of a PMMR device. The chapter begins with an overview of possible heat rejection measurement methods before presenting the selected method. Finally, the methods used to experimentally verify the proposed heat rejection measurement technique and key assumptions are explained.

3.1 Overview of Methods to Measure Heat Rejection

Measuring the rejected heat at the hot HEX is complex due to the transient flow of the HTF. A method of measuring heat rejection in steady state internal flow heat exchangers is to calculate the change in enthalpy of the fluid across the inlet and outlet as functions of the measured flow rate and temperature. Since the HTF is oscillating in the hot HEX, the mass flow rate and temperature at each opening vary with time. Thus, the commonly used steady state flow enthalpy equation (3.1) is difficult to use.

$$\Delta \dot{H} = \dot{m} c_p (T_{out} - T_{in}) \tag{3.1}$$

There are methods to measure heat transfer and heat flux through a material. Heat transfer from one point to another depends on the temperature difference between the two points and the thermal conductivities/resistances of the materials connecting them. Temperature can be measured using a variety of sensors including thermometers, thermocouples, thermistors, integrated circuit (IC) temperature sensors, and resistive temperature detectors (RTDs). The thermal resistance (R) is difficult to calculate with heat transfer theory due to the complex geometries and number of materials used in a typical HEX. Simulation can be used to estimate the thermal resistances

between the two flow regions; however, the accuracy of such an approximation should be verified using experimental data.

Heat flux sensors (HFSs) can measure the heat flux flowing through their cross-section. By directly measuring the heat transfer between the HTF and the chiller fluid using a HFS it is possible to characterize the heat transfer of the HEX. HFSs are thin pads which output a voltage proportional to the heat flux flowing normal to their surfaces [17]. HFSs are constructed from an array of series connected thermocouple junctions called a thermopile, which is woven between a thin material with a well-characterized thermal conductivity. Thermocouples exploit the Seebeck effect, a phenomenon in which two dissimilar metals will produce a voltage difference proportional to the junction temperature [18]. Figure 3.1 visualizes how the thermocouples are connected in series to create a thermopile, with 'hot' and 'cold' side junctions connected in reverse polarity. The resulting voltage from the thermopile is therefore proportional to the difference between the average temperature of each side, and thus the heat flux through the sensor.

$$V_{total} = (V_{H1} + V_{H2} + V_{H3}) - (V_{C1} + V_{C2} + V_{C3}) \sim T_H - T_C \sim \dot{Q}''$$
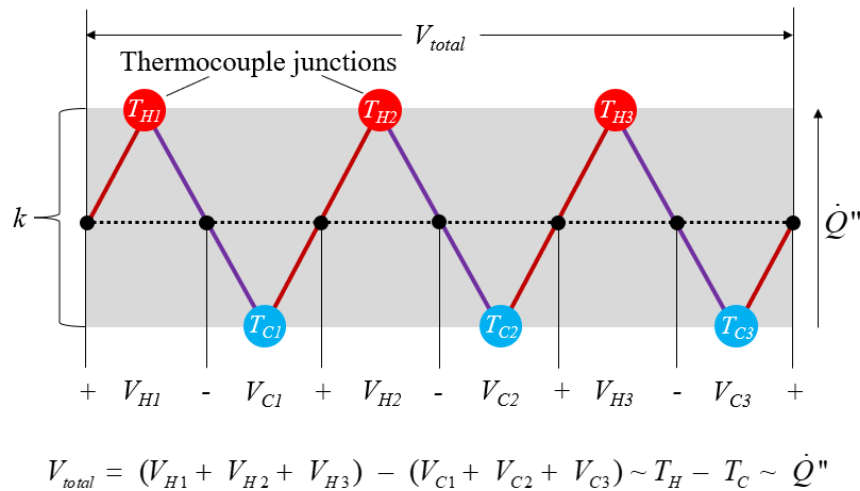
Figure 3.1: Diagram showing working principal of series connected thermopile heat flux sensor. All thermocouples are connected in series, with 'hot' and 'cold' side thermocouple junctions connected in reverse polarity. The resulting voltage V_{total} is proportional to the temperature difference between the two sides and thus the heat flux.

To maximize accuracy, it is important to minimize the impact of parallel heat transfer paths bypassing the HFS. Low conductivity materials can be used to insulate the HEX to the environment and to force as much heat as possible through the sensor. Figure 3.2 shows the proposed method

to force maximize the flow of rejected heat through the HFS using carefully placed insulation around a conductive aluminium network.
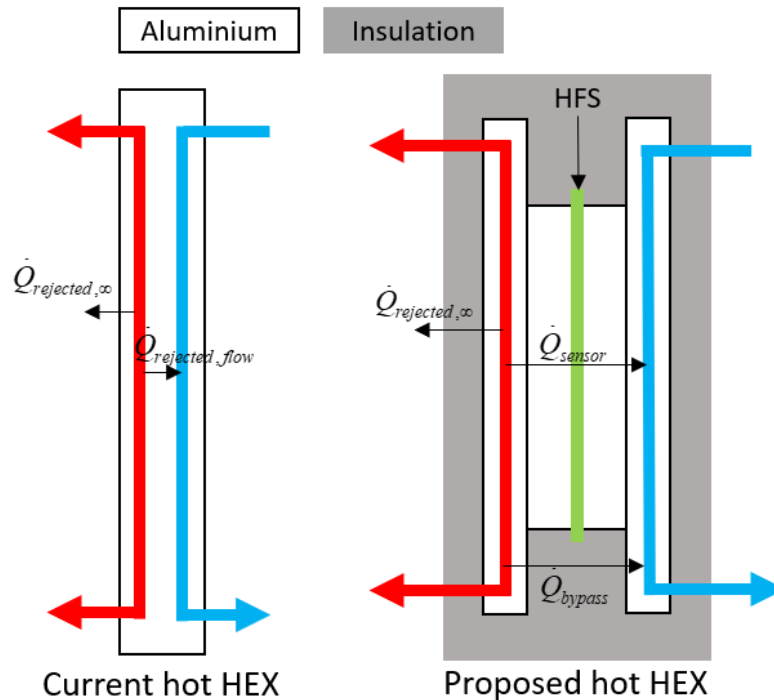
Figure 3.2: Simplified section view schematic showing the proposed heat exchanger modifications to measure rejected heat using a heat flux sensor. White boxes represent aluminium (conductive) parts, while grey areas represent insulating materials.

With this orientation some heat will still leak to the environment ($\dot{Q}_{rejected,\infty}$), and some of the heat exchanged between the hot and cold flows can be expected to bypass the HFS through the HEX components ($\dot{Q}_{bypass}$). To accurately measure the total heat rejection a method to characterize this bypassed and leaked heat is required.

3.2 Correlating Sensed Heat to Rejected Heat

Although the flow of the HTF in the hot HEX is transient, the fact that the flow is oscillating still allows for some simplifications. The oscillating flow will create oscillating heat fluxes in the materials near the flow region; however, further away from the flow field temperatures and heat fluxes are expected to remain relatively constant due to the thermal capacitance of the HEX parts. At very low operating frequencies the variance in heat fluxes could be significant throughout the

device, but PM1 and other MR devices typically operate between 1 and 5 Hz [15]. D'Esposito et al. [19] use equation (3.2) to determine the thermal penetration depth (δ) "defined as the distance that the heat diffuses through the material (under a sinusoidal stimulus) during a time $1/f$."

$$\delta = \sqrt{\frac{k}{c \cdot \rho \cdot \pi \cdot f}} \tag{3.2}$$

Where k, c and ρ are the thermal conductivity, specific heat capacity and density of the material respectively, and f is the frequency a sinusoidal heating operation is applied. Using this equation, the thermal penetration depth of an aluminium flow channel in a HEX operating at $f = 1$ Hz is 4.5mm, assuming perfect heat transfer between the HTF and flow channels, and using the properties of aluminium 6061 found in table c.4 in appendix C. Therefore, it is assumed that the heat rejection in the hot HEX can be treated as a steady state heat transfer problem resulting from transient flow if the HFS is placed at least 4.5mm from the flow channels.

To implement the assumption of constant heat rejection both fluids are treated as single temperature nodes computed by the average temperature of their inlets and outlets. The notation for these variables is described below in table 3.1, and the resulting circuit model is displayed in figure 3.3, which shows the current hot HEX equivalent circuit (left) and the proposed HFS configuration circuit (right).

Table 3.1: Descriptions of temperature variables.

Variable	Description
$\overline{T}_{H,fluid}$	Average hot fluid temperature (HTF).
$\overline{T}_{C,fluid}$	Average cold fluid temperature (chiller loop).
T_∞	Environmental temperature.
T_{sensor}	Temperature of HFS, measured by an integrated thermocouple.
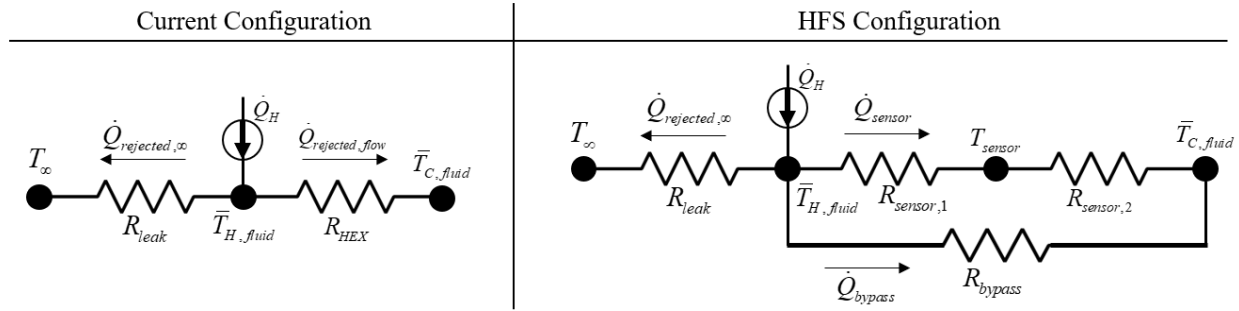
Figure 3.3: Thermal circuits of the existing PM1 hot HEX (left) and the HFS configured hot HEX (right).

The goal of this work is to measure the total rejected heat $\dot{Q}_H$, which can be broken up into three components by examining the HFS configuration circuit:

$$\dot{Q}_H = \dot{Q}_{sensor} + \dot{Q}_{rejected,\infty} + \dot{Q}_{bypass} \tag{3.3}$$

Since the HFS directly measures $\dot{Q}_{sensor}$, the only unknows of equation (3.3) are $\dot{Q}_{bypass}$ and $\dot{Q}_{rejected,\infty}$. It is possible to represent these unknowns as functions of temperature nodes if thermal resistance values are assumed constant (See section 5.3 for further discussion on thermal resistance variance).

$$\dot{Q}_{rejected} = \dot{Q}_{sensor}(\bar{T}_{H,fluid},\bar{T}_{C,fluid}) + \dot{Q}_{rejected,\infty}(\bar{T}_{H,fluid},T_\infty) + \dot{Q}_{bypass}(\bar{T}_{H,fluid},\bar{T}_{C,fluid})$$
$$\dot{Q}_{rejected} = f(\bar{T}_{H,fluid},\bar{T}_{C,fluid},T_\infty) \tag{3.4}$$

It should be noted that is also possible to replace $\bar{T}_{H,fluid}$ or $\bar{T}_{C,fluid}$ with T_{sensor}, since T_{sensor} is a function of $\bar{T}_{H,fluid}$ and $\bar{T}_{C,fluid}$. Thus, it is possible to write:

$$\dot{Q}_{rejected} = f(T_{sensor},\bar{T}_{C,fluid},T_\infty) \tag{3.5}$$

Where the total rejected heat is written as a function of the temperature of the sensor, chilled fluid, and environment. While this character equation does not depend on the heat sensed by the HFS ($\dot{Q}_{sensor}$), it should be noted that stream temperature is difficult and expensive to measure accurately. PM1 is currently fitted with thermocouples to monitor flow temperatures at various points; however, even the most accurate type T thermocouples offer accuracies of only $\pm 0.5°C$ at lower temperatures. While more accurate temperature sensors are available, it is very difficult to implement them into a compact MR system that must operate with an airtight internal flow at

pressures exceeding 550 *kPa* [20]. HFSs are accurate within ± 5%, so using a HFS despite the redundancy of the $\dot{Q}_{sensor}$ variable is expected to yield more accurate results. However, thermocouples can be used to approximate the fraction of heat passing through the sensor (f_s), which can be used to correlate sensed heat and rejected heat.

$$f_s = \frac{\dot{Q}_{sensor}}{\dot{Q}_H} = \frac{f(T_{sensor}, \bar{T}_{C,fluid})}{f(T_{sensor}, \bar{T}_{C,fluid}, T_\infty)}$$

(3.6)

$$\dot{Q}_H = \frac{1}{f_s} \cdot \dot{Q}_{sensor}$$

To validate these assumptions and derivations, a testbench HEX which implemented a HFS was designed and manufactured.

3.3 Testbench Device Experiment

To explore the proposed method of using a HFS to measure rejected heat in an oscillating flow HEX, a simplified device was designed and manufactured using isotropic materials and a symmetric layout. These design choices were made to allow for more simple simulation calculations. Figure 3.4 below shows a photograph of the assembled testbench HEX (left) along with an exploded rendering of one half of the symmetrical HEX (right). Two experiments were designed to correlate sensed heat and rejected heat, one which implemented a constant heat source using a resistive heating pad into the testbench HEX and another which implemented oscillating flow, as seen in MR devices. Figure 3.5 below shows a schematic of both the heating pad experiment (left) and the oscillating flow experiment (right). These experiments are further discussed throughout this section.
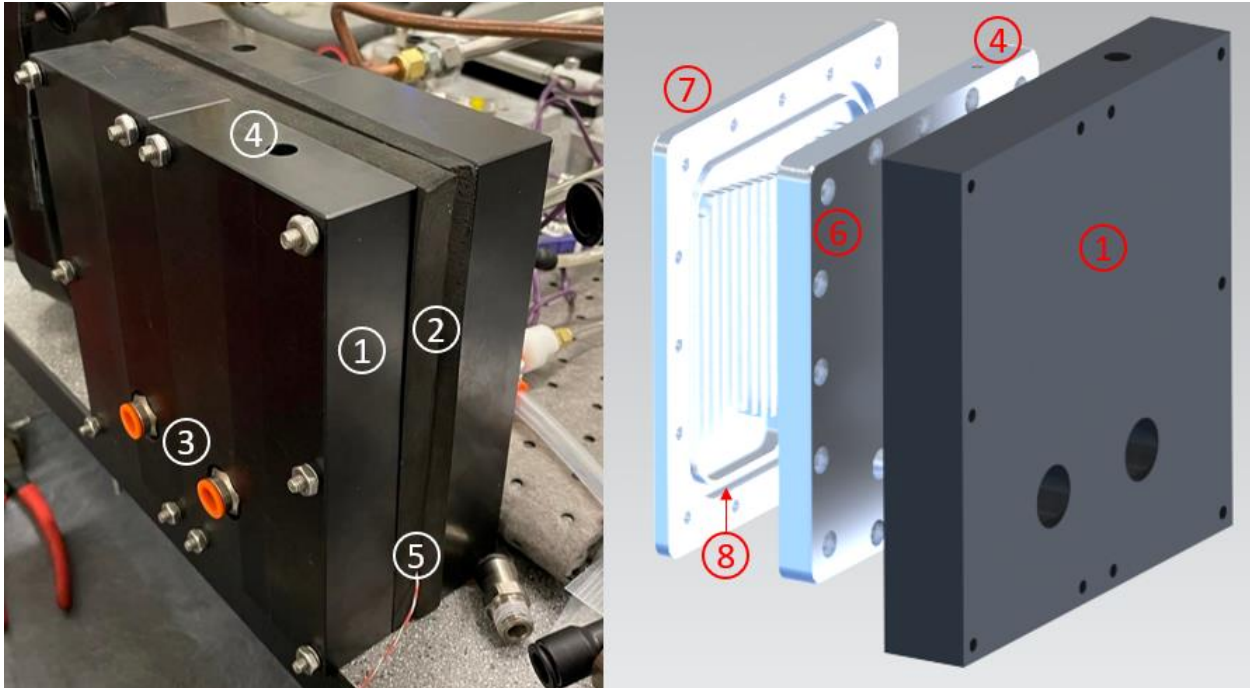
Figure 3.4: Testbench HEX assembled (left) and one half of the symmetrical device exploded view (right). (1) Delrin insulating cover, (2) EPDM foam insulation, (3) inlet/outlet, (4) air bleed valve, (5) HFS wiring, (6) flow region cover, (7) flow channels, (8) O-ring gland.
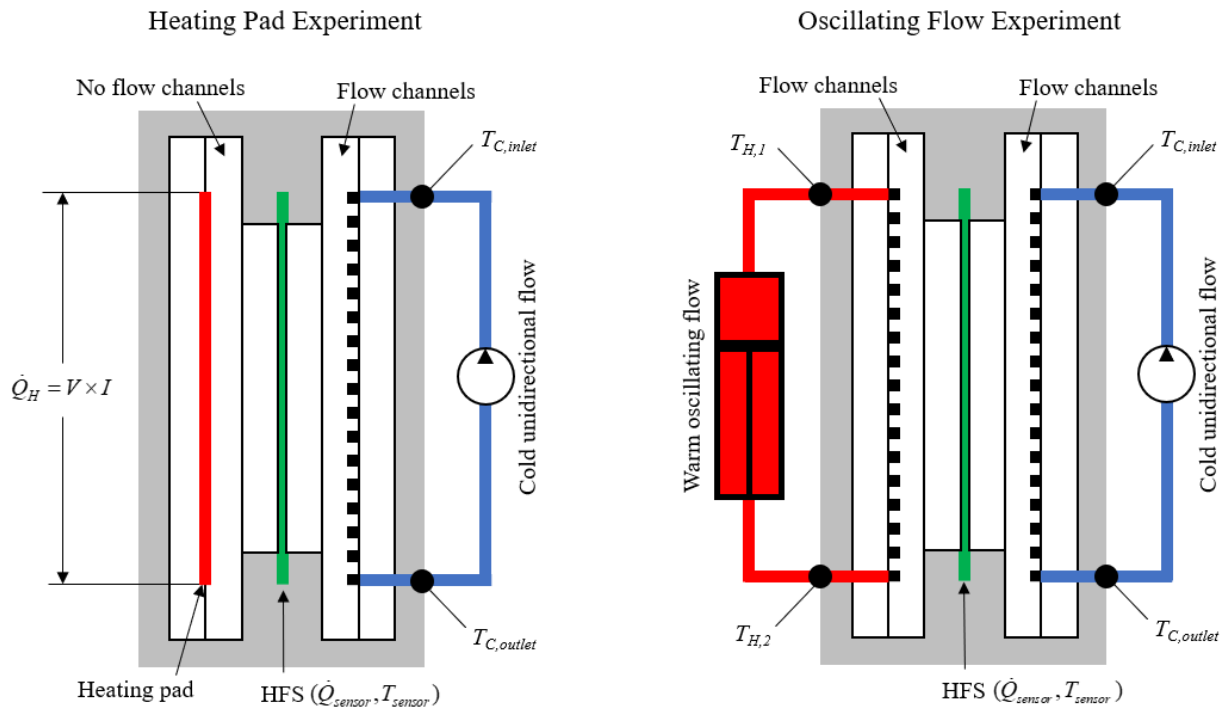
Figure 3.5: Diagrams showing the heating pad (left) and transient flow (right) experimental layouts performed on the testbench heat exchanger.

3.3.1 Experimental Procedure and Apparatus

To characterize the heat transfer in the oscillating flow HEX, the oscillating flow was first replaced with a constant and measurable heat source. A resistive heating pad was selected to simulate constant heat rejection since the input power is easily controlled and measured by the electrical power it is delivered. Running unidirectional steady state flow was also considered; however, type E thermocouples with $\pm\,1°C$ error are too inaccurate to measure a small temperature difference (typically $\Delta T_{in/out} \leq 2°C$). Even the most accurate type T thermocouples with errors of $\pm\,0.5°C$ would not be able to provide accurate measurements. Therefore, the flow channels were replaced with an identical part excluding the channels with a flat area to mount the resistive heating pad. During this heating pad experiment, the heater input voltage (V) was varied along with the cold stream inlet temperature ($T_{C,inlet}$) to effect the measurable independent variables rejected heat ($\dot{Q}_H$) and average cold stream temperature ($\overline{T}_{C,fluid}$). The sensed heat ($\dot{Q}_{sensor}$) and HFS temperature (T_{sensor}) were measured at various $\dot{Q}_H$ and $\overline{T}_{C,fluid}$ values. Using the data from this experiment, solutions to equation (3.5) and (3.6) where found for the testbench hot HEX.

To validate the assumptions of steady state heat rejection presented in section 3.2, oscillating flow was implemented into the testbench HEX. The average temperature of the hot oscillating fluid ($\overline{T}_{H,fluid}$) and the cold stream inlet temperature ($T_{C,inlet}$) were varied. The hydraulic displacer frequency (f) was kept constant at close to $1\ Hz$ to ensure the slowest oscillating system was considered. Like the heating pad experiment, the sensed heat ($\dot{Q}_{sensor}$) and HFS temperature (T_{sensor}) were measured at various $\overline{T}_{H,fluid}$ and $\overline{T}_{C,fluid}$ values. The motivation behind this experiment was to verify that the results would be consistent with the heating pad experiment. Matching results would indicate that heat rejection from an oscillating flow HEX can be characterized accurately using a HFS and a heating pad calibration.

The final apparatus is pictured below in figure 3.6, which shows a top view of the experimental apparatus used to induce oscillating flow in the testbench HEX along with the power supply used for the heating pad experiment.
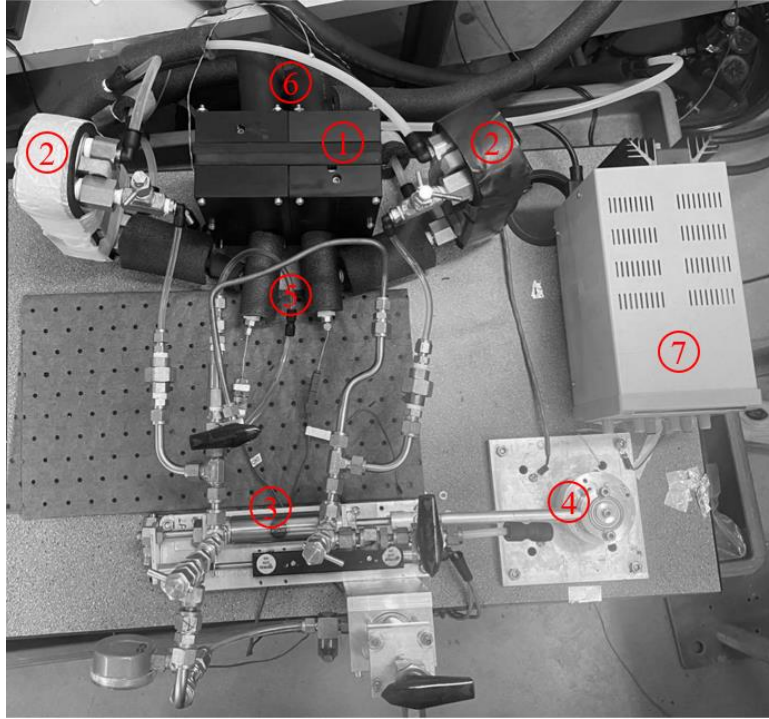
Figure 3.6: Experimental apparatus: (1) testbench HEX, (2) HEX's used to heat oscillating fluid, (3) hydraulic displacer, (4) crank mechanism, (5) oscillating fluid inlet/outlet, (6) chiller fluid inlet/outlet, (7) DC power supply for heating pad.

Table 3.2 below lists the variables considered in both experiments, and classifies them as 'user control', 'independent' or 'dependent'.

Table 3.2: Experimental variables.

Heating Pad Experiment		Oscillating Flow Experiment	
User control variables:	V & I, $T_{C,inlet}$	User control variables:	$\overline{T}_{H,fluid}$, $T_{C,inlet}$, f
Independent variables:	$\dot{Q}_H$, $\overline{T}_{C,fluid}$	Independent variables:	$\overline{T}_{C,fluid}$
Dependent variables:	$\dot{Q}_{sensor}$, T_{sensor}	Dependent variables:	$\dot{Q}_{sensor}$, T_{sensor}

While environmental temperature (T_∞) is a variable of the system, it was not controllable to a high degree of accuracy in the testing environment of this work. With excellent insulation environmental temperature fluctuations are expected to have minimal effect on the system; however, the effects of varying ambient temperatures were presented using simulation. The simulation methods used in this work are discussed in the next section, and further discussed in section 4.3 and further discussed in section 5.2.

3.3.2 Simulation

A steady state simulation model of the testbench HEX was created in Siemens NX. The purposes of the model were:

- To identify whether low resolution simulation can be used to accurately characterize the heat transfer in the HEX, eliminating the need for an experimental approach.
- To examine the effects of fluctuating environmental temperature.

The coupled thermal-flow simulation treats the testbench as a unidirectional counterflow HEX. This simplification derives from the underlying assumption in this work that an oscillating flow HEX can be assumed to have constant heat transfer. Other selected characteristics of the simulation included material properties, fluid properties and heat transfer facilitation (conductive couplings, convective properties).

First, the simulation characteristics were tuned to match experimental results. Material properties such as thermal conductivities, densities, etc. were set to known values from the literature. The area which required the most tuning was thermal coupling, as material interface resistances are not well documented and depend on a variety of conditions.

Following the tuning of thermal couplings, the final accuracy of the simulation was examined by comparing the simulation to experimental findings. The ambient temperature of the simulation was then varied to examine how fluctuations in environmental temperature could be expected to affect the final characterization of the HEX.

3.3.3 Methods of Data Analysis

Two planar least squares regressions (LSRs) were performed on the data set of the heating pad experiment. A LSR is a method of determining the best fit trendline by minimizing the square of the sum of the errors between each experimental data point and some trendline. This method was adapted to a three-dimensional system so that best fit regression planes could be found for both the sensed heat ($\dot{Q}_{sensor}$) and rejected heat ($\dot{Q}_H$) as functions of the average chiller fluid temperature ($\bar{T}_{C,fluid}$) and sensor temperature (T_{sensor}). Starting with the equation of a plane:

$$z = Ax + By + C \tag{3.7}$$

The distance between some ideal regression plane z_r and an experimental data point z_{exp} can be expressed as:

$$d = z_r - z_{\text{exp}} = Ax_i + By_i + C - z_{\text{exp}} \tag{3.8}$$

A least squares regression finds the values of *A*, *B* and *C* that minimize the sum of the distances between some ideal regression and experimental data. The distances are squared to eliminate the negative values resulting from equation (3.8). The function that should be minimized can be written as:

$$LS(A,B,C) = \sum_{i=1}^{n} d^2 = \sum_{i=1}^{n} (Ax_i + By_i + C - z_{\text{exp},i})^2 \tag{3.9}$$

The function can be minimized by solving for the values of *A*, *B* and *C* at which the gradient of *LS(A,B,C)* is equal to zero. Therefore, the following matrix equation can be derived:

$$\nabla(LS) = 0 \rightarrow
\begin{bmatrix}
\sum_{i=1}^{n} x_i^2 & \sum_{i=1}^{n} x_i y_i & \sum_{i=1}^{n} x_i \\
\sum_{i=1}^{n} x_i y_i & \sum_{i=1}^{n} y_i^2 & \sum_{i=1}^{n} y_i \\
\sum_{i=1}^{n} x_i & \sum_{i=1}^{n} y_i & n
\end{bmatrix}
\begin{bmatrix} A \\ B \\ C \end{bmatrix}
=
\begin{bmatrix}
\sum_{i=1}^{n} x_i z_{\text{exp},i} \\
\sum_{i=1}^{n} y_i z_{\text{exp},i} \\
\sum_{i=1}^{n} z_{\text{exp},i}
\end{bmatrix} \tag{3.10}$$

And finally, the planar constants *A*, *B* and *C* are solved for:

$$
\begin{bmatrix} A \\ B \\ C \end{bmatrix}
=
\begin{bmatrix}
\sum_{i=1}^{n} x_i^2 & \sum_{i=1}^{n} x_i y_i & \sum_{i=1}^{n} x_i \\
\sum_{i=1}^{n} x_i y_i & \sum_{i=1}^{n} y_i^2 & \sum_{i=1}^{n} y_i \\
\sum_{i=1}^{n} x_i & \sum_{i=1}^{n} y_i & n
\end{bmatrix}^{-1}
\begin{bmatrix}
\sum_{i=1}^{n} x_i z_{\text{exp},i} \\
\sum_{i=1}^{n} y_i z_{\text{exp},i} \\
\sum_{i=1}^{n} z_{\text{exp},i}
\end{bmatrix} \tag{3.11}$$

This process was computed for both the sensed heat ($\dot{Q}_{sensor}$) and rejected heat ($\dot{Q}_H$) as functions of the average chiller fluid temperature ($\overline{T}_{C,fluid}$) and sensor temperature (T_{sensor}), resulting in planes of the form:

$$\dot{Q}_{sensor}(T_{sensor}, \overline{T}_{C,fluid}) = A_s \overline{T}_{C,fluid} + B_s T_{sensor} + C_s$$
$$\dot{Q}_H(T_{sensor}, \overline{T}_{C,fluid}) = A_r \overline{T}_{C,fluid} + B_r T_{sensor} + C_r \tag{3.12}$$

These planes can then be substituted into equation (3.6) to find f_s and complete the correlation between sensed heat and rejected heat. The coefficient of determination (R^2) can then be used to measure how well the model fits the data set. R^2 is a unitless fraction between zero and one. If $R \approx 1$, the regression plane can be considered an excellent predictor of the dependent variable. The coefficient of determination is found by equation (3.13), which measures the fraction of explained variance:

$$R^2 = 1 - \frac{\sum_{i=1}^{n}(z_{\exp,i} - z_{r,i})^2}{\sum_{i=1}^{n}(z_{\exp,i} - \overline{z}_{\exp})^2} \tag{3.13}$$

Where $\overline{z}_{\exp}$ is the average of all experimental z values. This R^2 value is used in this work to test the validity of the regression planes which are generated in the form of equation (3.12).

This chapter began with an explanation of the methods proposed in this work to measure rejected heat ($\dot{Q}_H$) using a HFS. The chapter then described the test apparatus, experimental procedure, simulation practices and data analysis methods used to verify the proposed method. Chapter 4 will display the results from the procedures discussed.

Chapter 4

Results

This chapter displays the results from the heating pad and oscillating flow experiment and examines the results of the CFD and thermal simulation. For both experiments at least 45 minutes between experiments was required to ensure the HEX reached steady state. In total, 67 experimental data points were collected (28 heating pad and 39 oscillating flow). The full data set is available in Appendix A.

4.1 Heating Pad Experiment

With the heating pad configuration previously discussed and shown in Figure 3.5, the input heat ($\dot{Q}_H$) and the chilling loop temperature ($\overline{T}_{C,fluid}$) were varied 28 times. The resulting HFS temperature and heat flux were measured. Table 4.1 below summarizes the key independent and dependent variables of this experiment, and Figure 4.1 below displays the results from the LSR performed on the data set. The entire data set can be found in Table A.2 of appendix A.

Table 4.1: Variables examined during the heating pad experiment.

Independent Variables		Dependent Variables	
Heating pad input:	$\dot{Q}_H$ [W]	HFS heat:	$\dot{Q}_{sensor}$ [W]
Chilled flow inlet temperature:	$\overline{T}_{C,fluid}$ [°C]	HFS temperature:	T_{sensor} [°C]
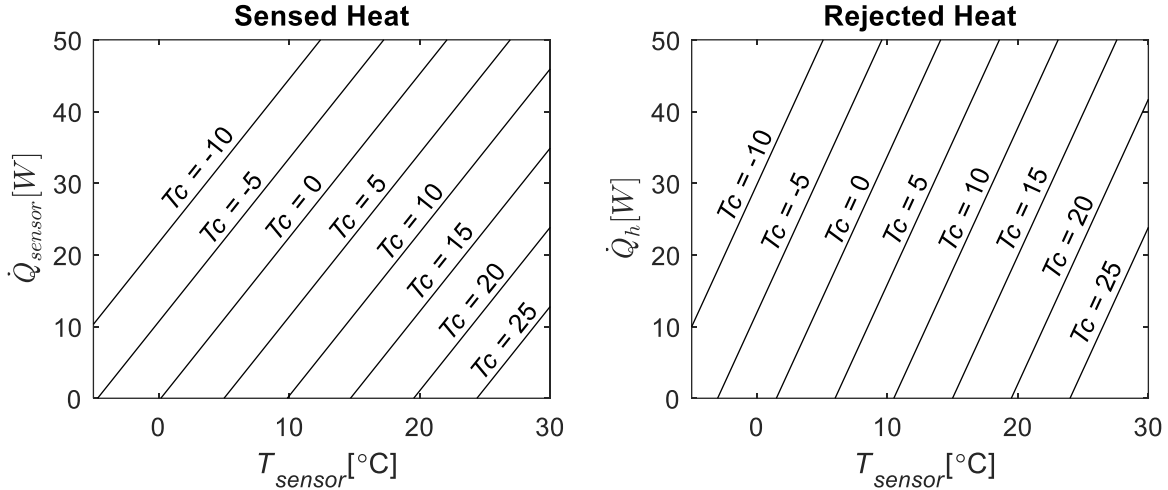
Figure 4.1: Resulting planar least squares regression from the heating pad experiment. Heat measured by the sensor (left) and total heat rejection simulated by the heating pad (right). Each linear line represents a slice of the corresponding regression plane taken in 5°C increments of $\overline{T}_{C,fluid}$.

The LSR performed on the heating pad data set is further defined in section 4.4. Next, the HEX was switched to the oscillating flow configuration.

4.2 Oscillating Flow Experiment

With the oscillating flow experimental configuration, the hot and cold flow temperatures were varied and data was collected 39 times. An operating frequency of 0.95 Hz was used for all data points. Table 4.2 below summarizes the key independent and dependent variables of this experiment, and the entire data set can be found in Table A.3 of appendix A.

Table 4.2: Variables examined during the oscillating flow experiment.

Independent Variables		Dependent Variables	
Hot flow temperature:	$\overline{T}_{H,fluid}$ [°C]	HFS heat:	$\dot{Q}_{sensor}$ [W]
Chilled flow inlet temperature:	$\overline{T}_{C,fluid}$ [°C]	HFS temperature:	T_{sensor} [°C]

The LSR performed on the heating pad data set was compared to the oscillating flow data as discussed previously in section 3.3.3 is further defined in section 4.4. Next, several simulation data points were collected and compared to experimental data.

4.3 Simulation

Coupled thermal-flow simulation was performed using Siemens NX on an assembly model of the testbench HEX. After 22 iterations of tuning contact resistances, the simulation interface contact resistances shown in table 4.3 were found to produce results comparable to experimental findings. It should be noted that while these contact resistances allowed the simulation to produce results comparable to experimental results, these contact resistances were selected somewhat arbitrarily through a random tuning process and do not necessarily represent reality.

Table 4.3: Simulation interface contact resistance values found to produce results comparable to experimental findings.

Interface	Simulation value	Literature value
Aluminium/aluminium*	0.6 $K/(kW/m^2)$	0.15-0.5 $K/(kW/m^2)$ [21]
Delrin/aluminium	8 $K/(kW/m^2)$	N/A
EPDM/aluminium	2 $K/(kW/m^2)$	N/A
EPDM/Delrin	3 $K/(kW/m^2)$	N/A
HFS (FluxTeq PHFS-09e)**	4 $K/(kW/m^2)$	~0.9 $K/(kW/m^2)$

*Incropera et al. provide aluminium/aluminium interfaces with $100kN/m^2$ contact pressure, while contact pressure was not considered in this work. Therefore, resistances may vary.
**HFS thermal resistivity approximated by manufacturer does not include contact resistance between aluminium HEX parts.

A total of 9 simulations were performed to verify the correlation between simulated and experimental values. The chiller fluid and HTF inlet temperatures were varied so that trends could be examined. Figure 4.2 below displays the results for $\dot{Q}_H$ (a) and f_s (b) for all 9 simulations compared to the experimental results.
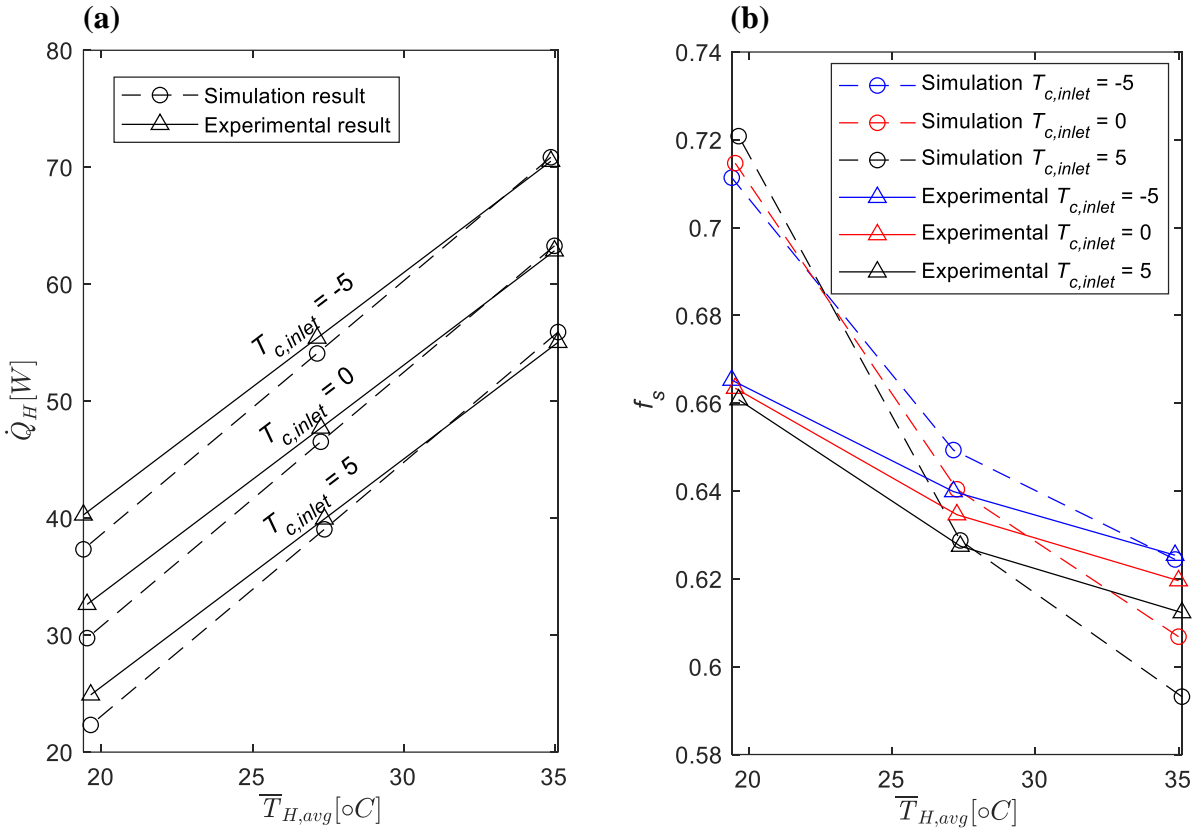
Figure 4.2: Comparison of simulation results to experimental results. (a) shows the calculation of rejected heat, and (b) shows the calculation of the sensed heat fraction.

Next, the effects of varying environmental temperature were examined using the simulation environment. The chiller fluid inlet temperature ($T_{c,in}$) was set to 0°C for all points tested, and the HTF and environmental temperatures were changed to a cooler (18°C) and warmer (25°C) 'room temperature', to see how this would vary from average laboratory conditions of 20.8°C. Figure 4.3 below shows the resulting trends for $\dot{Q}_H$ (a) and f_s (b).

(a)

(b)
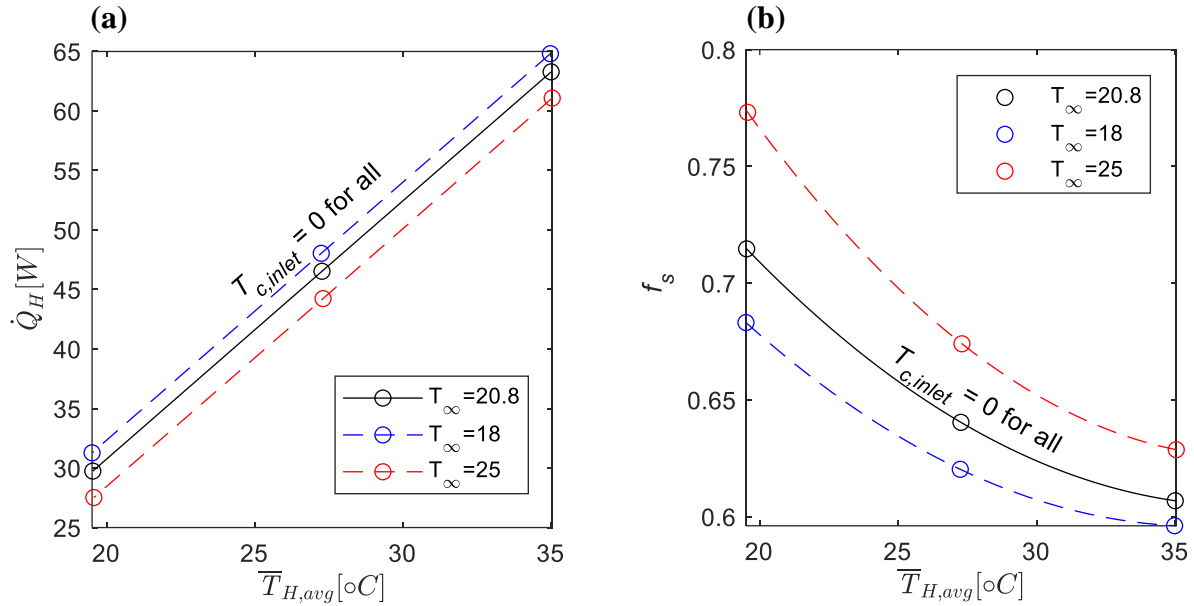
Figure 4.3: Simulation results from varying ambient temperature. (a) shows the simulation results for rejected heat at three different ambient temperatures, and (b) displays the simulated sensed heat fraction. $T_{c,in}$ is set to 0°C for all data.

The average laboratory temperature measured throughout the experimental phase of this project was 20.8°C, although the temperature was found to fluctuate between approximately 20°C and 22°C regularly. Additional simulations were performed at these environmental temperatures, and the data is presented in figure 4.4 below.
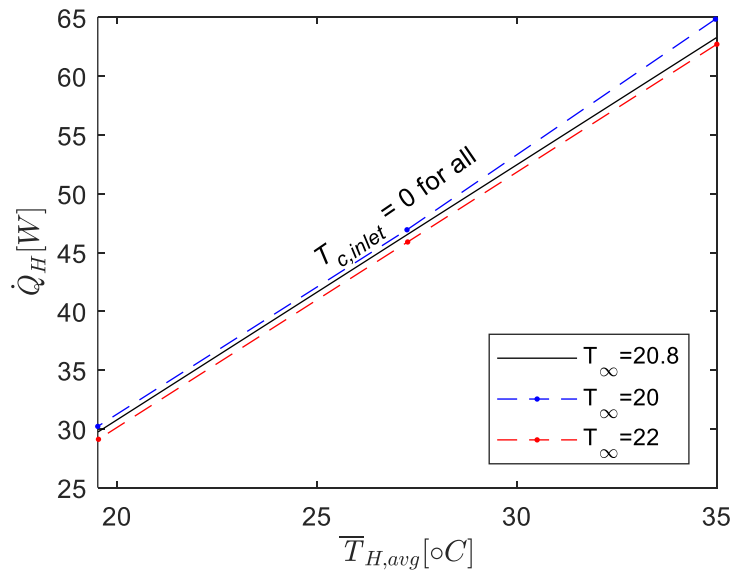
Figure 4.4: Simulated effects of varying $T\infty$ between 20°C and 22°C according to average measured laboratory conditions.

4.4 Final Characterization

A LSR was performed on sampled data points to calculate a planar regression for the sensed heat ($\dot{Q}_{sensor}$) and the input heat ($\dot{Q}_H$).

$$\frac{\dot{Q}_{sensor}}{\dot{Q}_H} = f_s = \frac{A_s \overline{T}_{c,fluid} + B_s T_{sensor} + C_s}{A_r \overline{T}_{c,fluid} + B_r T_{sensor} + C_r} \tag{4.1}$$

Where *A, B* and *C* are the planar constants calculated by the planar regression for the sensed heat plane and rejected heat plane, and f_s is the fraction of total rejected heat that is directly measured.

Table 4.4: Characterization constants to calculate rejected heat.

Sensed Heat Plane		Rejected Heat Plane	
A_s	-2.21	A_r	-3.57
B_s	2.28	B_r	3.97
C_s	-0.38	C_r	-5.91

And finally, the rejected heat $\dot{Q}_H$ can be written in two forms:

Form 1: In the form of equation (3.5) using only thermocouples.

$$\dot{Q}_H = -3.57 \cdot \overline{T}_{c,fluid} + 3.97 \cdot T_{sensor} - 5.91 \tag{4.2}$$

Form 2: In the form of equation (3.6) using thermocouples and the HFS.

$$\dot{Q}_H = \frac{1}{f_s} \cdot \dot{Q}_{sensor} = \left(\frac{-3.57 \cdot \overline{T}_{c,fluid} + 3.97 \cdot T_{sensor} - 5.91}{-2.21 \cdot \overline{T}_{c,fluid} + 2.28 \cdot T_{sensor} - 0.38} \right) \dot{Q}_{sensor} \tag{4.3}$$

Figure 4.5 below shows the sensed heat fraction (f_s) as a function of T_{sensor} at various $\overline{T}_{C,fluid}$ (written as T_c in the figure).
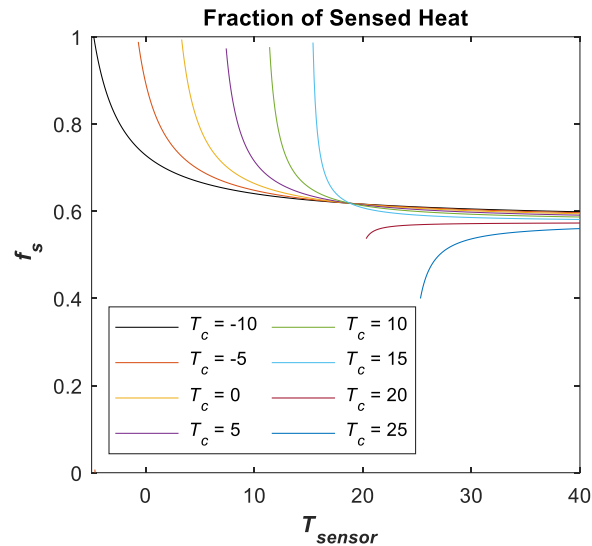
Figure 4.5: Fraction of sensed heat (f_s) at various sensor (T_{sensor}) and cold stream temperatures (T_C, referred to in the text as $\overline{T}_{C,fluid}$) determined by equation (4.1).

Next, the coefficient of determinations (R^2) were examined. The heating pad data set was compared to both the sensed heat and rejected heat regression planes to verify the data fit the planar regression well, and then the oscillating flow data set was compared to the sensed heat plane to verify that oscillating flow can be assumed to have constant heat rejection. Table 4.5 below lists the R^2 value that was calculated by comparing the data set listed in the left column to the regression plane listed in the middle column.

Table 4.5: Coefficient of determination of each data set compared to a corresponding regression plane.

Data set	Regression plane	R^2
Heating pad	$\dot{Q}_{sensor}$	0.999
Heating pad	$\dot{Q}_H$	0.995
Oscillating flow	$\dot{Q}_{sensor}$	0.993

This chapter displayed the results from the experimental and simulation efforts performed on the testbench heat exchanger. The following chapter will go into more detail about the key findings of this data and the potential sources of error.

Chapter 5

Discussion of Results

This chapter discusses the results displayed in Chapter 4 of this thesis, including some of the key findings as well as the imperfections and sources of error in the model.

5.1 Experimental Findings

All data sets were found to fit their corresponding LSR plane. First, comparing the heating pad experimental data to the resulting regression planes of $\dot{Q}_H$ and $\dot{Q}_{sensor}$ resulted in R^2 values of 0.995 and 0.999 respectively. This shows that the regression planes represent the experimental data from the heating pad experiment almost perfectly. Secondly, comparing the oscillating flow experimental data to the $\dot{Q}_{sensor}$ LSR plane generated by heating pad experimental data was found to have an R^2 value of 0.993. This suggests that the heating pad experiment produced the same results as the oscillating flow experiment and proves that the heating pad method of characterizing an oscillating flow heat exchanger is dependable. This also validates the assumption first introduced in section 3.2 that quickly oscillating flow can be treated to have steady state heat rejection.

The planar relationships between heat transfer and temperature were not surprising due to the theoretical linear relationship between heat transfer and temperature gradient. The thermal conductivity of the heat transfer fluid varies with temperature; however, the overall change in thermal resistance appears negligible due to the highly planar trend in the data. This is further examined in section 5.3 below.

The rejected heat $\dot{Q}_H$ was written in two forms, first with only thermocouple inputs and second with both thermocouple and HFS inputs (equation (4.2) and (4.3) respectively). While it is expected that the second form be more accurate as previously discussed in section 3.2, vertical asymptotes are present as the sensor temperature approaches the chilled fluid temperature. Around these asymptotes higher sensitivities to sensor inaccuracies can be expected. The impacts of these asymptotes on the accuracy of the model are further discussed in section 5.4 below.

5.2 Simulated Findings

It should be recalled that the NX simulation was created with the following purposes:

- To identify whether low resolution simulation can be used to accurately characterize the heat transfer in the HEX, eliminating the need for an experimental approach.
- To examine the effects of fluctuating environmental temperature.

In this section, the simulation's ability to satisfy these purposes is discussed by reflecting on the results displayed in section 4.3.

5.2.1 Characterizing HEX Heat Rejection

After 22 iterations, the contact resistances of the materials were tuned to produce results comparable to experimental findings as shown in figure 4.2. The contact resistances between each HEX part were found to have significant impacts on the rejected heat ($\dot{Q}_H$) and the sensed heat fraction (f_s). Unfortunately, contact resistances are not well defined in the literature as they rely heavily on surface finish and contact pressure. The contact resistances shown in table 4.3 were tuned arbitrarily to replicate experimental values for $\dot{Q}_H$ and $\dot{Q}_{sensor}$ at different T_{sensor} and $\overline{T}_{C,fluid}$ values. Therefore, it is unclear whether these simulation contact resistance values represent real world values. Because of the significant impact part interface thermal resistances have on simulation results and the lack of literature indicating what these values might be, results suggest that simulation should not be used as a replacement to the experimental method of characterizing hot HEX rejected heat.

5.2.2 Examining the Effects of Fluctuating Ambient Temperature

The average temperature in the characterization environment was measured to be 20.8 °C, with regular fluctuations around approximately 20°C - 22°C. Ambient temperature can be very different

to control in a laboratory setting, although its impacts are clear by examining the heat transfer circuit shown previously in figure 3.3. For example, if the ambient temperature is higher than average, $\dot{Q}_H$ can be expected to be lower than the model predicted value, since the heat rejected to the environment ($\dot{Q}_{rejected,\infty}$, a function of $\overline{T}_{C,fluid}$ and T_∞) will be less. Consequently, $\dot{Q}_{sensor}$ can be expected to remain relatively constant, which will result in a higher f_s. This trend was captured by the simulation and is best shown in figure 4.3. Under standard laboratory conditions as shown in figure 4.4, the simulation showed that approximately $\pm 0.5W$ of error can be expected due to fluctuating environmental temperature when measuring $\dot{Q}_H$. With improved insulation, this error could be decreased further. A limited amount of simulation data was analyzed in this work, although in future work this error could be fully characterized into an equation of the form:

$$\dot{Q}_H = \dot{Q}_{sensor} \cdot \frac{A_r \overline{T}_{c,fluid} + B_r T_{sensor} + C_r}{A_s \overline{T}_{c,fluid} + B_s T_{sensor} + C_s} + f(T_\infty) \tag{5.1}$$

Where $f(T_\infty)$ is some correcting function of environmental temperature. With the limited simulation data presented in this thesis, a characterization of this function is not possible and unnecessary due to the small error band of $\pm 0.5W$ resulting from fluctuating environmental temperature. It can be concluded that simulation can be an effective way of estimating the minor impact of small fluctuations in environmental temperature.

This section discussed the simulation data presented in Chapter 4 of this thesis and identified the low-resolution simulation used as an effective method of approximating the effects of varying ambient temperature, but not as an effective way of accurately characterizing the expected heat rejection of a MR hot HEX.

5.3 Thermal Resistance Variance with Temperature

It should be noted that all resistance values noted in this work (R_{sensor}, R_{leak}, R_{bypass}) have some variance depending on the internal flow temperatures. The flow of both the HTF and chiller fluid was found to be laminar, with maximum Reynold's number of 1600 at peak operating frequencies. Using laminar internal heat flow correlations the convection coefficient between the flow channels and the water-glycol mix can be determined with [21], [22]:

$$h_{conv} = \frac{Nu \bullet k}{D_h} \tag{5.2}$$

Where *Nu* is the Nusselt number – a function of the Reynolds and Prandtl number. Assuming constant heat flux between the fluid and the flow channels a Nusselt number of 3.61 should be used. The hydraulic diameter (D_h) can be written as dependent on the cross-sectional area of the pipe (A_c) and the wetted perimeter (P).

$$D_h = \frac{4A_c}{P} \tag{5.3}$$

Using the temperature dependent functions found by Trevizoli [23] (full equations available in Appendix B), the average convection coefficient between the HTF (20% ethylene glycol, 80% water mix) and the flow channels was determined as a function of fluid temperature. Figure 5.1 below shows the theoretical thermal resistance associated with the convection of heat between the aluminium flow channels and the chiller fluid on the left, and the total resistance between the HFS and the chiller fluid on the right.
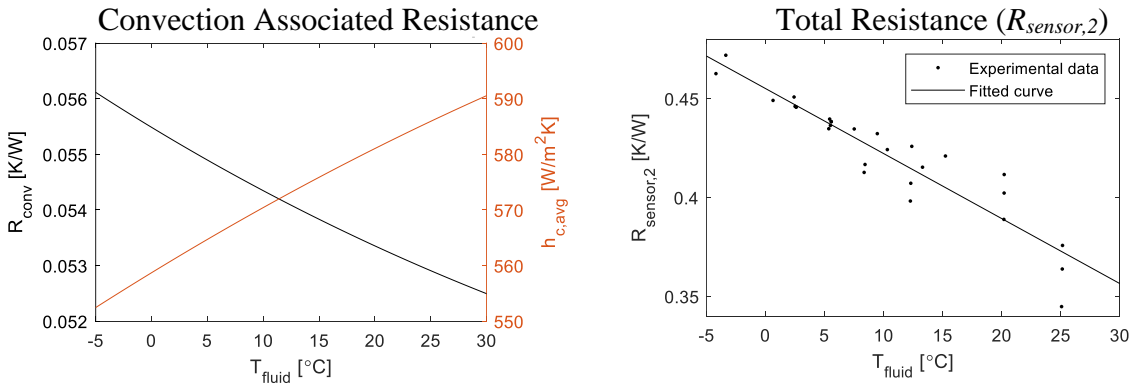
Figure 5.1: Comparing the theoretical resistance associated with convection at the cold side of the HEX (R_{conv}, left) with the measured total thermal resistance between the HFS and cold flow ($R_{sensor,2}$, right).

The thermal resistance between the fluid and the flow channels only accounts for approximately 12% of the total thermal resistance between the sensor and the cold flow ($R_{sensor,2}$) at any given temperature. Additionally, the theoretical difference in convective resistance between the chiller fluid aluminum flow channels is only about 0.004 K/W across the 35°C interval shown, while a change of about 0.1 K/W is shown by the data. Therefore, the variance in convection associated

resistance accounts for an insignificant amount of the change in total thermal resistance and can be neglected as a non-linearity.

Another factor expected to induce varying resistance with respect to temperature is thermal expansion of HEX parts. Warmer parts will expand, causing firmer contact with interfacing parts. Contact resistances between the HEX parts are unknown, but it is shown in the literature that increasing contact pressure at interfaces decreases thermal resistance significantly [21]. Thermal expansion is likely to make up a significant portion of the variance in thermal resistances, as there are few alternate possibilities. Regardless, the data was found to follow planar trends nearly perfectly, so varying thermal resistance can be neglected in the model.

5.4 Instrumentation Error

One significant source of error in the measurement of hot HEX heat rejection is the accuracy of the sensors used. Recalling the derived equations equation (4.2) and (4.3) which can be used to estimate heat rejection using sensor data:

Form 1: Using only thermocouples.

$$\dot{Q}_H = -3.574 \cdot \overline{T}_{c,fluid} + 3.970 \cdot T_{sensor} - 5.914 \tag{4.2}$$

Form 2: Using thermocouples and the HFS.

$$\dot{Q}_H = \left(\frac{-3.574 \cdot \overline{T}_{c,fluid} + 3.970 \cdot T_{sensor} - 5.914}{-2.209 \cdot \overline{\overline{T}}_{c,fluid} + 2.280 \cdot T_{sensor} - 0.380} \right) \dot{Q}_{sensor} \tag{4.3}$$

Realizing that $\overline{T}_{C,fluid}$, T_{sensor} and $\dot{Q}_{sensor}$ are required to estimate $\dot{Q}_H$, the measurement accuracies of the sensors used to measure these variables must be examined. Table 5.1 below lists the instruments that were used to measure these variables and their error bounds.

Table 5.1: Critical variables measurement methods and error bounds.

Variable	Measurement Method	Error
$\overline{T}_{c,fluid}$	Thermocouple (Type E)	$\pm 1.0\ °C$
T_{sensor}	Thermocouple (Type T)	$\pm 0.5\ °C$
$\dot{Q}_{sensor}$	Heat flux sensor	$\pm 5\ \%$

Since thermocouple error is absolute and HFS error is relative, the error will vary depending on the location of the test point. The instrumentation inaccuracies were input into form 1 (thermocouple measurement) and form 2 (HFS measurement) to find the maximum errors at various operating points. It was noted that at low $\dot{Q}_H$ values the form 2 equation exhibited a large spike in measurement error about a vertical asymptote due to the division term in equation (4.3). This asymptote is shown in figure 5.2 below, which displays potential measurement results of the worst case 'negative' error scenario of both equation forms.
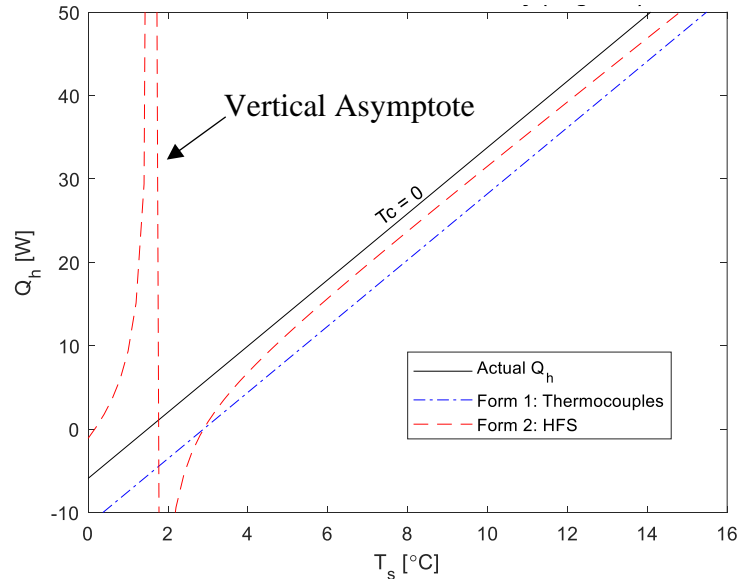
Figure 5.2: Maximum negative error measuring $\dot{Q}_h$ using thermocouples only compared to using the HFS measurement. The chart only displays $\overline{T}_{c,fluid} = 0°C$ for readability, and shows the right shifted vertical asymptote.

These results suggest that at low heat rejection values very large errors could be expected, and prompted a more thorough analysis at various $\overline{T}_{C,fluid}$ and T_{sensor} values. The worst-case error scenario measuring $\dot{Q}_H$ using both equation forms was evaluated for a wide range of T_{sensor} and $\overline{T}_{C,fluid}$ values. Both relative and absolute error were examined to determine the ranges in which each equation form should be used. The results of this analysis are displayed as a colour plot below in figure 5.3. The top two images are the relative error of form 1 (left) and form 2 (right), and the bottom two images are the absolute error of form 1 (left) and form 2 (right). Regions with error above the indicated value are plotted in black, and dotted white lines indicated $\dot{Q}_H$ values. The solid white line represents the point at which $\dot{Q}_H = 0$, therefore the region below this line represents negative heat rejection and can be ignored.
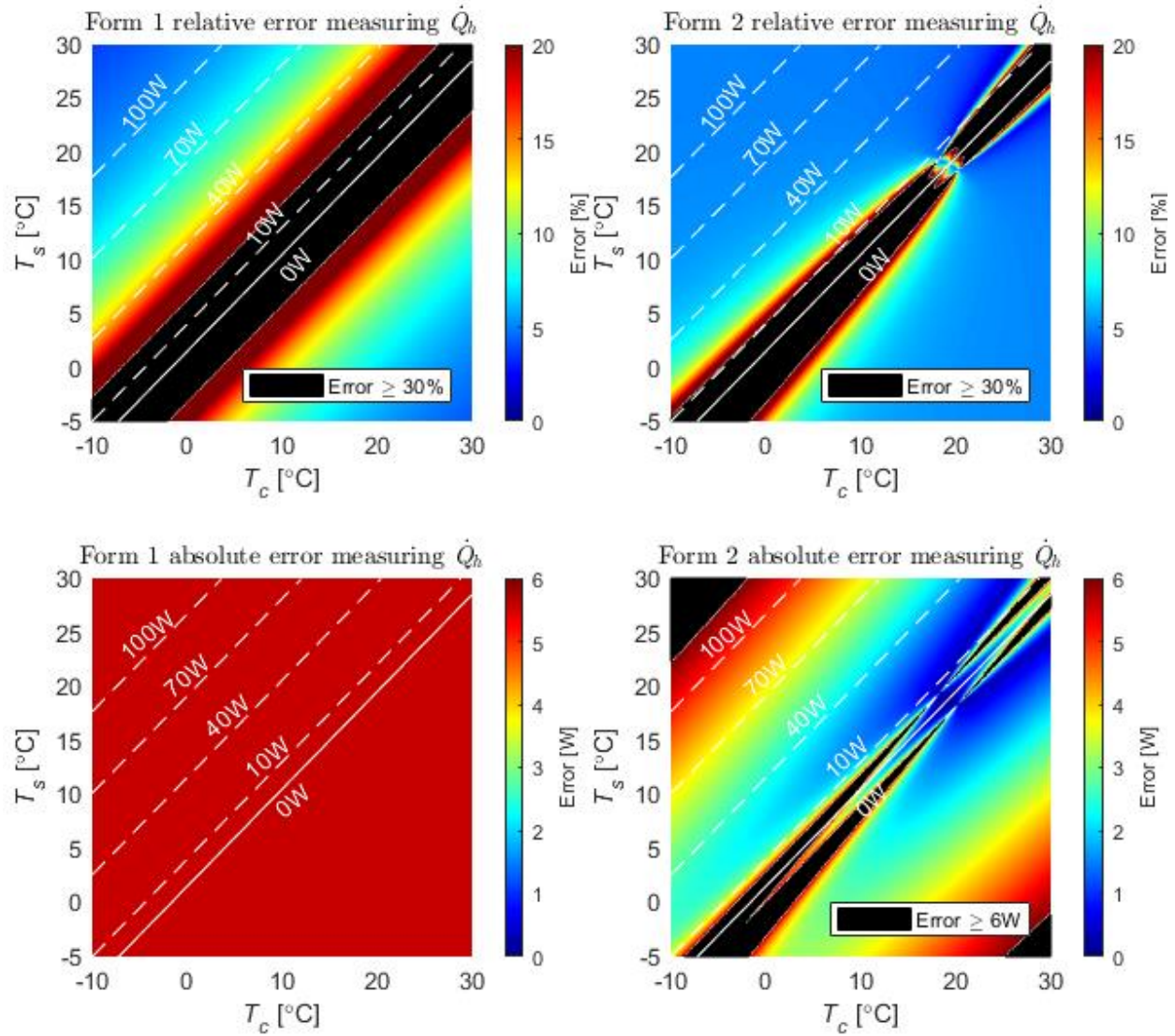
Figure 5.3: Maximum relative (top two) and absolute (bottom two) errors when measuring $\dot{Q}_H$ using the form 1 equation (thermocouple only, left two) compared to the form 2 equation (thermocouple and HFS, right two). The solid white line represents the points where $\dot{Q}_H = 0\text{W}$, and the dotted lines represent their labelled heat rejection values. The area below the 0 W line represents negative heat rejection (not applicable to a PMMR hot HEX). $T_s = T_{sensor}$, and $T_c = \bar{T}_{C,fluid}$.

There are several interesting findings presented by the instrument error analysis shown in figure 5.3. First, the monochromatic chart showing form 1's absolute error (see bottom left image) shows that the absolute error of form 1 is consistently $\pm 5.6W$. This results in large relative errors at lower heat rejection values, which become less considerable as heat rejection increases (see top left image). It can also be seen that the potential errors of form 2 are lower than form 1 at lower heat rejection values, which can be seen by comparing the top left and top right figures. The black area

representing errors greater than 30% exists until approximately $10W$ of heat rejection using form 2, while errors over 30% can be expected until about $20W$ of heat rejection using form 1. Finally, it should be noted that at high values of heat rejection form 1 becomes more accurate. This can be seen by comparing the absolute error (bottom figures), in which a black region is seen on the upper corner of the form 2 figure. This shows that the relative accuracy of form 1 is more accurate beyond heat rejection values of approximately $110W$. Table 5.2 below summarizes the findings above and lists the most accurate correlation to use for a corresponding range of heat rejection. It should be noted that the listed ranges will vary depending on the HEX and instrumentation used. The best way to improve heat rejection measurement accuracy is to use more accurate HFSs or temperature sensors.

Table 5.2: Characterization formula accuracy bounds. Listed ranges will vary depending on the HEX and instrumentation used.

Range ($\dot{Q}_H$)	Recommended Correlation
$0 - 10W$	N/A – errors greater than 30%
$10 - 110W$	Form 2
$110W +$	Form 1

This chapter discussed the findings of the results, as well is the main sources of error. The following chapter will summarize and conclude this thesis and provide some recommendations for future work on this topic.

Chapter 6

Conclusions and Recommendations

This section summarizes the work discussed in this report and provides implementation and future work recommendations with some final thoughts.

6.1 Summary

Magnetic refrigeration (MR) is an alternate refrigeration method which uses environmentally benign materials, eliminating the need for a carbon intensive refrigerant. A MR cycle exploits the magnetocaloric effect (MCE), a phenomenon in which certain magnetocaloric materials (MCMs) will heat up significantly when subjected to a magnetic field. The MCE is applied at the active magnetic regenerator (AMR) which houses the MCM. To conduct efficient and meaningful research on MR it is necessary to isolate and quantify the performance of the AMR region of the device. It was shown that the AMR coefficient of performance COP_{AMR} can be found by measuring the rejected heat $\dot{Q}_H$ at the hot HEX of an MR device. The proposed method to measure $\dot{Q}_H$ is to place a heat flux sensor at the hot HEX between the warm heat transfer fluid and the external cooling fluid with careful insulation around the HEX. With this layout, it is possible to correlate the measured heat to the total heat rejection using equation (3.6). Although the heat transfer fluid flows transiently through the HEX, steady heat rejection can be assumed due to its relatively quick oscillation. Because of this realization, it was possible to experimentally determine the fraction of total rejected heat flowing through the heat flux sensor at various cooling loop temperatures by using a heating pad to simulate a constant heat rejection $\dot{Q}_H$ in place of the heat transfer fluid.

6.2 Recommendations and Future Work

The approach taken in this work was found to be extremely accurate, and it is recommended that MR devices with research purposes be retrofitted with hot HEXs capable of heat rejection measurement. This capability will allow consistent and meaningful performance calculations which can be compared across studies. The recommended process is as follows:

1. Implement a HFS between the hot and cold side, with insulation to the environment and between bypass routes.
2. Replace transient flow region with a heating pad and follow the heating pad experiment procedure examined in this paper. To speed up this characterization process it is recommended that data only be collected at the edges of the design space (see section 3.3.1).
3. Fit a planar regression to collected data and derive the coefficients A, B and C for the rejected and sensed heat planes (see section 3.3.3).
4. Determine the accuracy ranges of both form 1 and form 2 equations and implement this into the DAQ system (see section 5.4).
5. Implement the new HEX in the MR system.

Future work on this topic should further examine the effects of environmental temperature and seek an approach to include this variable in the system. The slight effects of environmental temperature variation are noted throughout the study and examined more closely with simulation. A future study using a similar HEX in an environment with a more controllable temperature could provide some method to include this variable in the system.

6.3 Conclusion

The objective of this work was to provide a method to isolate and quantify the performance of a regenerator in a MR system. Arnold et. al. [9] had previously derived the COP_{AMR} value which satisfied this objective; however, the methods used by Arnold et. al. to measure this value was not simple to implement on any MR device around the world – specifically Halbach orientation PMMR devices. It was found that the COP_{AMR} value of any PMMR device could be measured by measuring the rejected heat from the hot HEX.

This thesis proposed measuring the rejected heat using a HFS placed between the hot and cold side of the HEX. Accurate measurement of rejected heat meant that the heat bypassing the sensor needed to be characterized. An experimental procedure was designed to correlate the sensed heat to the total rejected heat as a function of the cold fluid temperature and the HFS temperature. Using a resistive heating pad in place of the oscillating fluid as a controllable and measurable 'heat rejection' source, it was possible to characterize the rejected heat at various device operating points.

The method proposed in this thesis was found to have high accuracy at higher heat rejection values, and lower accuracy at low heat rejection values due to instrumental error. The accuracy varies depending on the operating point; however, methods to determine the accuracy at any point are presented. The effects of varying environmental temperature were examined using a small set of simulated data. It was found that with environmental temperature variance of $\pm 1°C$ errors in measuring $\dot{Q}_H$ can be estimated to be $\pm 0.5W$. It is recommended that future work more closely examines the effects of varying environmental temperature and attempt to provide a method to implement it as a variable in the characterization equations.

References

[1]   International Institute of Refrigeration, "The impact of the refrigeration sector on climate change," *35th Inf. Note Refrig. Technol.*, 2017.

[2]   G. Dreyfus *et al.*, "Assessment of Climate and Development Benefits of Efficient and Climate-Friendly Cooling," 2020. [Online]. Available: https://ccacoalition.org/en/resources/assessment-climate-and-development-benefits-efficient-and-climate-friendly-cooling.

[3]   R. Ciconkov, "Refrigerants: There is still no vision for sustainable solutions," *Int. J. Refrig.*, vol. 86, pp. 441–448, 2018, doi: 10.1016/j.ijrefrig.2017.12.006.

[4]   G. V. Brown, "Magnetic heat pumping near room temperature," *J. Appl. Phys.*, vol. 47, no. 8, pp. 3673–3680, 1976, doi: 10.1063/1.323176.

[5]   B. Vieira, "Magnetocaloric properties of spheroidal La(Fe,Mn,Si)$_{13}$H$_y$ granules and their performance in epoxy-bonded active magnetic regenerators," *Appl. Therm. Eng.*, vol. 183, 2020, [Online]. Available: https://doi.org/10.1016/j.applthermaleng.2020.116185.

[6]   T. V Christiaanse, "Characterization, Experimentation and Modeling of Mn-Fe-Si-P Magnetocaloric Materials.," 2009.

[7]   J. Liang, "Performance assesment of a triangular microchannel active magnetic regenerator," *Appl. Therm. Eng.*, vol. 186, 2021, [Online]. Available: https://doi.org/10.1016/j.applthermaleng.2020.116519.

[8]   P. V. Trevizoli, "Thermal-hydraulic evaluation of 3D printed microstructures," *Appl. Therm. Eng.*, vol. 160, 2019, [Online]. Available: https://doi.org/10.1016/j.applthermaleng.2019.113990.

[9]   D. S. Arnold, A. Tura, and A. Rowe, "Experimental analysis of a two-material active

magnetic regenerator," *Int. J. Refrig.*, vol. 34, pp. 178–191, 2011, doi: 10.1016/j.ijrefrig.2010.08.015.

[10] J. Barbosa Jr, J. Lozano, and P. Trevizoli, "Magnetocaloric Refrigeration Research at the INCT in Cooling and Thermophysics," Florianopolis, 2014. [Online]. Available: http://polo.ufsc.br/portal/images/files/MAGNETOCALORIC REFRIGERATION THERMOPHYSICS_JADER_PAULO_JAIME.pdf.

[11] D. S. Arnold, A. Tura, A. Ruebsaat-Trott, and A. Rowe, "Design improvements of a permanent magnet active magnetic refrigerator," *Int. J. Refrig.*, vol. 37, pp. 99–105, 2014, [Online]. Available: http:/dx.doi.org/10.1016/j.ijrefrig.2013.09.024.

[12] R. Teyber, P. V. Trevizoli, T. V. Christiaanse, P. Govindappa, I. Niknia, and A. Rowe, "Permanent magnet design for magnetic heat pumps using total cost minimization," *J. Magn. Magn. Mater.*, vol. 442, pp. 87–96, 2017, doi: 10.1016/j.jmmm.2017.06.039.

[13] M. Masche, J. Liang, K. Engelbrecht, and C. R. H. Bahl, "Performance assessment of a rotary active magnetic regenerator prototype using gadolinium," *Appl. Therm. Eng.*, vol. 204, Dec. 2021, Accessed: May 26, 2022. [Online]. Available: https://doi.org/10.1016/j.applthermaleng.2021.117947.

[14] A. Rowe, "Configuration and performance analysis of magnetic refrigerators," *Int. J. Refrig.*, vol. 34, no. 1, pp. 168–177, 2011, doi: 10.1016/j.ijrefrig.2010.08.014.

[15] A. Tura and A. Rowe, "Permanent magnet magnetic refrigerator design and experimental characterization," *Int. J. Refrig.*, vol. 34, pp. 628–639, 2011, doi: 10.1016/j.ijrefrig.2010.12.009.

[16] A. Tura, J. Roszmann, J. Dikeos, and A. Rowe, "Cryogenic Active Magnetic Regenerator Test Apparatus," 2006, doi: 10.1063/1.2202511.

[17] D. J. Rossouw, "Point Temperature Measurements," *Appl. Thermo-Fluidic Meas. Tech. An Introd.*, pp. 169–190, Jan. 2016, doi: 10.1016/B978-0-12-809731-1.00006-X.

[18] A. Immonen, S. Levikari, F. Gao, M. Kuisma, and P. Silventoinen, "MEMS Heat Flux Sensor," Lappeenranta, 2020. [Online]. Available: http://arxiv.org/abs/2006.02808.

[19] R. D'Esposito, S. Balanethiram, J. L. Battaglia, S. Fregonese, and T. Zimmer, "Thermal Penetration Depth Analysis and Impact of the BEOL Metals on the Thermal Impedance of SiGe HBTs," *IEEE Electron Device Lett.*, vol. 38, no. 10, pp. 1457–1460, 2017, doi: 10.1109/LED.2017.2743043.

[20] T. V Christiaanse, "Pressure behavior in an active magnetic regenerator test apparatus," Victoria, 2015.

[21] F. Incropera, D. Dewitt, T. Bergman, and A. Lavine, *Fundamentals of Heat and Mass Transfer*, 6th ed., vol. 112. Wiley, 2015.

[22] R. S. Subramanian, "Heat transfer in Flow Through Conduits," 2006.

[23] P. Trevizoli, "Technical Report for water-glycol mixtures," Victoria, 2012.

[24] B. Zirnstein, D. Schulze, and B. Schartel, "Mechanical and Fire Properties of Multicomponent Flame Retardant EPDM Rubbers Using Aluminum," *Materials (Basel).*, vol. 12, no. 1932, pp. 1–22, 2019.

Appendix A

Experimental Data Set

This appendix provides the full set of experimental data collected in the heating pad and oscillating flow experiments. All data was acquired with a sampling frequency of 75 *Hz*, averaged over 10 seconds. Approximately 45 minutes was allowed after changing set fluid temperatures for the HEX parts to reach steady state. Steady state conditions were further verified by ensuring the rate of change of the sensor temperature was approximately zero ($dT_{sensor} \approx 0$). Table A.1 below summarizes the experimental variables used in this work and the error bounds of the instruments used to measure them.

Table A.1: Summary of experimental variables and their uncertainties.

Variable	Symbol	Uncertainty
Heating pad voltage	V	± 0.10 V
Heating pad current	I	± 0.01 A
Rejected heat	$\dot{Q}_H$	$\%\text{Err}(V) + \%\text{Err}(I)$
Cold side temperatures	$T_{C,in}$, $T_{C,out}$, $\bar{T}_{C,fluid}$	± 1.0 °C
Hot side temperatures	$T_{H,1}$, $T_{H,2}$, $\bar{T}_{H,fluid}$	± 1.0 °C
Sensor temperature	T_{sensor}	± 0.5 °C
Sensor heat flux	$\dot{Q}_{sensor}$	$\pm 5\%$

The measured results of these variables during the heating pad and oscillating flow experiment are displayed in sections A.1 and A.2 below.

A.1 Heating Pad

Table A.2 below displays the experimental results from the heating pad experiment introduced in section 3.3.1.

Table A.2: Experimental results from the heating pad experiment.

V [V]	I [A]	$\dot{Q}_H$ [W]	$T_{C,in}$ [°C]	$T_{C,out}$ [°C]	$\overline{T}_{C,fluid}$ [°C]	$\dot{Q}_{sensor}$ [W]	T_{sensor} [°C]
7.19	1.41	10.14	2.3	2.6	2.4	8.13	6.1
7.21	1.41	10.17	5.2	5.5	5.4	7.51	8.6
7.26	1.41	10.24	8.3	8.4	8.4	7.27	11.4
7.32	1.42	10.39	12.2	12.3	12.3	7.12	15.1
7.69	1.52	11.69	-3.6	-3.2	-3.4	10.69	1.7
7.81	1.51	11.79	20.2	20.2	20.2	7.29	23.0
7.86	1.51	11.87	25.1	25.1	25.1	6.24	27.4
7.88	1.52	11.98	25.1	25.0	25.1	5.54	27.0
9.13	1.78	16.25	8.3	8.5	8.4	10.98	13.0
9.18	1.78	16.34	12.2	12.4	12.3	10.34	16.5
9.50	1.83	17.39	25.1	25.2	25.2	8.73	28.4
10.41	2.01	20.92	20.2	20.3	20.2	12.22	25.1
10.6	2.08	22.05	-4.5	-3.9	-4.2	16.32	3.4
12.38	2.40	29.71	15.1	15.4	15.2	17.90	22.8
12.97	2.53	32.81	2.3	2.9	2.6	21.37	12.1
12.97	2.53	32.81	2.3	2.9	2.6	21.37	12.1
13.06	2.55	33.30	5.3	5.8	5.6	21.00	14.8
13.06	2.55	33.30	5.3	5.8	5.6	21.00	14.8
13.19	2.56	33.77	9.3	9.7	9.5	21.04	18.6
13.29	2.55	33.89	20.1	20.3	20.2	19.17	28.1
13.19	2.57	33.90	7.3	7.7	7.5	21.19	16.7
13.31	2.58	34.34	12.2	12.6	12.4	20.63	21.2
14.06	2.73	38.38	5.2	5.8	5.5	24.14	16.0
13.98	2.73	38.17	0.3	0.9	0.6	25.04	11.9
10.02	1.97	19.74	2.3	2.7	2.5	14.46	9.0
10.06	1.97	19.82	5.3	5.6	5.4	13.92	11.6
12.08	2.32	28.03	10.2	10.5	10.3	17.48	17.7
11.32	2.18	24.68	13.2	13.4	13.3	15.11	19.6

A.2 Oscillating Flow

Table A.3 below displays the experimental results from the oscillating flow experiment introduced in section 3.3.1.

Table A.3: Experimental results from the oscillating flow experiment.

$T_{H,1}$ [°C]	$T_{H,2}$ [°C]	$\bar{T}_{H,fluid}$ [°C]	$T_{C,in}$ [°C]	$T_{C,out}$ [°C]	$\bar{T}_{C,fluid}$ [°C]	$\dot{Q}_{sensor}$ [W]	T_{sensor} [°C]
24.5	24.9	24.7	2.9	2.3	2.6	23.29	13.2
25.5	25.7	25.6	5.7	5.2	5.5	21.19	15.0
26.2	26.5	26.4	7.6	7.2	7.4	19.71	16.4
26.9	27.2	27.0	9.6	9.2	9.4	18.76	17.6
28.4	28.6	28.5	12.5	12.2	12.4	17.18	19.7
30.1	30.3	30.2	17.3	17.2	17.2	13.89	23.1
31.2	31.3	31.2	20.3	20.2	20.2	11.80	25.0
31.8	31.9	31.9	22.2	22.1	22.1	10.36	26.3
33.0	33.1	33.0	25.2	25.2	25.2	8.18	28.4
27.6	28.0	27.8	2.9	2.3	2.6	26.89	14.6
28.4	28.8	28.6	5.7	5.2	5.5	24.55	16.4
29.5	29.8	29.6	8.8	7.7	8.2	22.17	18.7
30.0	30.3	30.1	10.6	9.5	10.0	21.23	19.8
30.8	31.1	31.0	12.4	12.1	12.3	19.98	20.9
31.5	31.8	31.7	14.4	14.1	14.2	18.26	22.2
32.6	32.8	32.7	17.4	17.1	17.2	16.68	24.2
33.7	33.8	33.8	20.3	20.1	20.2	14.50	26.2
34.0	34.2	34.1	22.2	22.2	22.2	12.41	27.2
35.5	35.6	35.5	25.2	25.1	25.1	10.99	29.5
11.5	11.7	11.6	-3.9	-4.5	-4.2	16.81	3.6
13.4	14.0	13.7	1.7	1.2	1.5	12.94	7.4
14.7	14.9	14.8	5.6	5.3	5.4	10.20	9.9
16.4	16.5	16.5	10.3	10.1	10.2	6.82	13.2
18.1	18.0	18.1	15.2	15.1	15.2	3.36	16.4
15.8	16.1	16.0	1.0	0.4	0.7	16.43	8.0
17.6	17.7	17.7	5.7	5.3	5.5	13.17	11.3
19.2	19.4	19.3	10.4	10.2	10.3	9.95	14.5
20.9	21.0	21.0	15.3	15.2	15.2	6.19	17.7
18.6	18.8	18.7	1.0	0.5	0.8	19.09	9.3
20.1	20.3	20.2	5.8	5.3	5.5	15.45	12.4

22.0	22.1	22.1	10.6	10.3	10.4	12.56	15.7
23.7	23.9	23.8	15.4	15.2	15.3	9.28	19.0
25.6	25.7	25.6	20.2	20.2	20.2	5.71	22.4
17.1	17.4	17.3	-3.8	-4.5	-4.1	22.87	6.3
21.5	21.8	21.6	1.1	0.5	0.8	22.37	10.7
23.3	23.5	23.4	5.8	5.3	5.6	19.26	14.0
25.1	25.3	25.2	10.7	10.3	10.5	16.17	17.4
26.7	26.8	26.8	15.5	15.3	15.4	12.52	20.5
28.3	28.4	28.4	20.3	20.2	20.3	9.02	23.7

Appendix B

Water-Glycol Properties

This appendix displays the formulas and code used to calculate the properties of water-glycol solution at varying temperatures. All equations and parameters found in this section are derived and characterized by Trevizoli [23].

Trevizoli found polynomial functions that can be used to approximate the density (ρ), specific heat (c_p), thermal conductivity (k) and viscosity (μ) of water-glycol as a function of the temperature (T) and mixture fraction (*%wt*). Using pure water as a reference, correction factors can be calculated using the equations below. The desired water-glycol property can be found by multiplying the reference and correction property together, as shown in equation (B.1).

$$x_{mix}(T,\% wt) = x_{ref} \cdot x_{correction} \tag{B.1}$$

Where *T* is the fluid temperature in Kelvin, and *%wt* is the mass fraction of glycol in the mixture. For example, if 20% of the mass of the mixture was glycol, *%wt* would equal 0.2.

1. Density ρ [kg/m^3]

The density of water-glycol can be estimated using the following reference and correction functions.

$$\rho_{ref} = -517 + 14.3 \cdot T - 4.40 \times 10^{-2} \cdot T^2 + 4.38 \times 10^{-5} \cdot T^3 \tag{B.2}$$

$$\rho_{correction} = \frac{(a - b \cdot T + c \cdot T^2 - d \cdot T^3 - e \cdot \% wt - f \cdot \% wt^2)}{(1 - g \cdot T + h \cdot T^2 - i \cdot T^3 - j \cdot \% wt)} \tag{B.3}$$

With the following constants:

$$
\begin{aligned}
a &= 1.09 & f &= 6.01 \times 10^{-4} \\
b &= 1.02 \times 10^{-2} & g &= 9.43 \times 10^{-3} \\
c &= 3.13 \times 10^{-5} & h &= 2.89 \times 10^{-5} \\
d &= 3.26 \times 10^{-8} & i &= 3.04 \times 10^{-8} \\
e &= 2.52 \times 10^{-2} & j &= 1.83 \times 10^{-2}
\end{aligned}
$$

2. Specific heat capacity c_p [J/kg-K]

The specific heat capacity of water-glycol can be estimated using the following reference and correction functions.

$$
\begin{aligned}
c_{p,ref}(T < 293K) &= 2.45 \cdot 10^5 - 2.50 \cdot 10^3 \cdot T + 8.67 \cdot T^2 - 1.00 \cdot 10^{-2} \cdot T^3 \\
c_{p,ref}(T \geq 293K) &= 4184
\end{aligned}
\tag{B.4}
$$

$$
\begin{aligned}
c_{p,correction} &= a - \frac{b}{T} + c \cdot \%wt + \frac{d}{T^2} - e \cdot \%wt^2 - \frac{f \cdot \%wt}{T} - \frac{g}{T^3} - h \cdot \%wt^3 \\
&\quad + \frac{i \cdot \%wt^2}{T} + \frac{j \cdot \%wt}{T^2}
\end{aligned}
\tag{B.5}
$$

With the following constants:

$$
\begin{aligned}
a &= 15.6 & f &= 1060 \\
b &= 1.33 \times 10^4 & g &= 4.05 \times 10^8 \\
c &= 1.79 & h &= 0.164 \\
d &= 4.02 \times 10^6 & i &= 125 \\
e &= 0.433 & j &= 1.30 \times 10^5
\end{aligned}
$$

3. Thermal conductivity k [W/m-K]

The thermal conductivity of water-glycol can be estimated using the following reference and correction functions.

$$k_{ref} = -0.681 + 6.88 \times 10^{-3} \cdot T - 8.71 \times 10^{-6} \cdot T^2 \tag{B.6}$$

$$k_{correction} = \frac{\left(a - b \cdot T - c \cdot \%wt - d \cdot T^2 + e \cdot \%wt^2 + f \cdot T \cdot \%wt\right)}{\left(1 - g \cdot T + h \cdot \%wt - i \cdot T^2 - j \cdot \%wt^2 - k \cdot T \cdot \%wt\right)} \tag{B.7}$$

$a =$ 0.769　　　　$g =$ 7.80×10^{-3}

$b =$ 6.49×10^{-3}　　$h =$ 0.110

$c =$ 2.86　　　　$i =$ 1.99×10^{-6}

$d =$ 4.05×10^{-6}　　$j =$ 0.205

$e =$ 6.02×10^{-2}　　$k =$ 2.96×10^{-3}

$f =$ 1.06×10^{-2}

4. Dynamic viscosity μ [kg/m-s]

The dynamic viscosity of water-glycol can be estimated using the following reference and correction functions.

$$\mu_{ref} = 0.799 - 9.76 \times 10^{-3} \cdot T + 4.50 \times 10^{-5} \cdot T^2 - 9.23 \times 10^{-8} \cdot T^3 + 7.13 \times 10^{-11} \cdot T^4 \tag{B.8}$$

$$\mu_{correction} = \frac{-a + b \cdot T - c \cdot T^2 - d \cdot \%wt - e \cdot \%wt^2}{1 - f \cdot T + g \cdot T^2 - h \cdot T^3 + i \cdot \%wt} \tag{B.9}$$

With the following constants:

$a =$ 0.481　　　　$f =$ 1.05×10^{-2}

$b =$ 3.17×10^{-3}　　$g =$ 3.63×10^{-5}

$c =$ 5.58×10^{-6}　　$h =$ 4.23×10^{-8}

$d =$ 4.39×10^{-2}　　$i =$ 2.66×10^{-2}

$e =$ 8.31×10^{-2}

Appendix C

Simulation Parameters and Results

This appendix discusses some of the key parameters used to create the NX simulation model, along with some colour plots generated in the results file. Table C.4 below lists the material properties used in the NX simulation of the testbench HEX. The table includes the thermal conductivity (k), density (ρ), specific heat (c_p) and dynamic viscosity (μ).

Table C.4: Material properties used for testbench HEX simulation.

Material	k (W/m·K)	ρ (kg/m^3)	c_p (J/kg·K)	μ (mPa·s)
Water/glycol (80/20 mix)*	0.51	1029	3920	1.72
Aluminium 6061**	154	2700	896	-
Delrin	0.50	1420	1470	-
EPDM foam	0.29 [24]	100	1800	-

*All water/glycol properties treated as a function of temperature. Listed property is at 20°C, formulas used found in Appendix B.
**Aluminium 6061 default properties provided by NX. Listed thermal conductivity (k) is at 20°C but treated as a function of temperature, while density (ρ) and specific heat (c_p) are constant.

The internal flow simulation used a no-slip wall condition with NX automatic convection properties and a mixing length turbulence model. Surface convection to the environment was calculated using inclined and horizontal plate convection, which automatically calculates convection coefficients using the material properties, gravitational constant and part geometry. A 3D tetrahedral mesh of the HEX was used, with a size of 8*mm* (NX automatically varies mesh size near small features). Thermal contact resistances used were previously stated in table 4.3.

Figure C.1 below displays an example of colour plots generated by the NX simulation. The images show the outer HEX temperature, the fluid temperature, a section view of conductive heat flux and a section view of the temperature.

Device Temperature [℃]

Fluid Temperature [℃]

Section View - Conductive Heat Flux [W/cm^2]
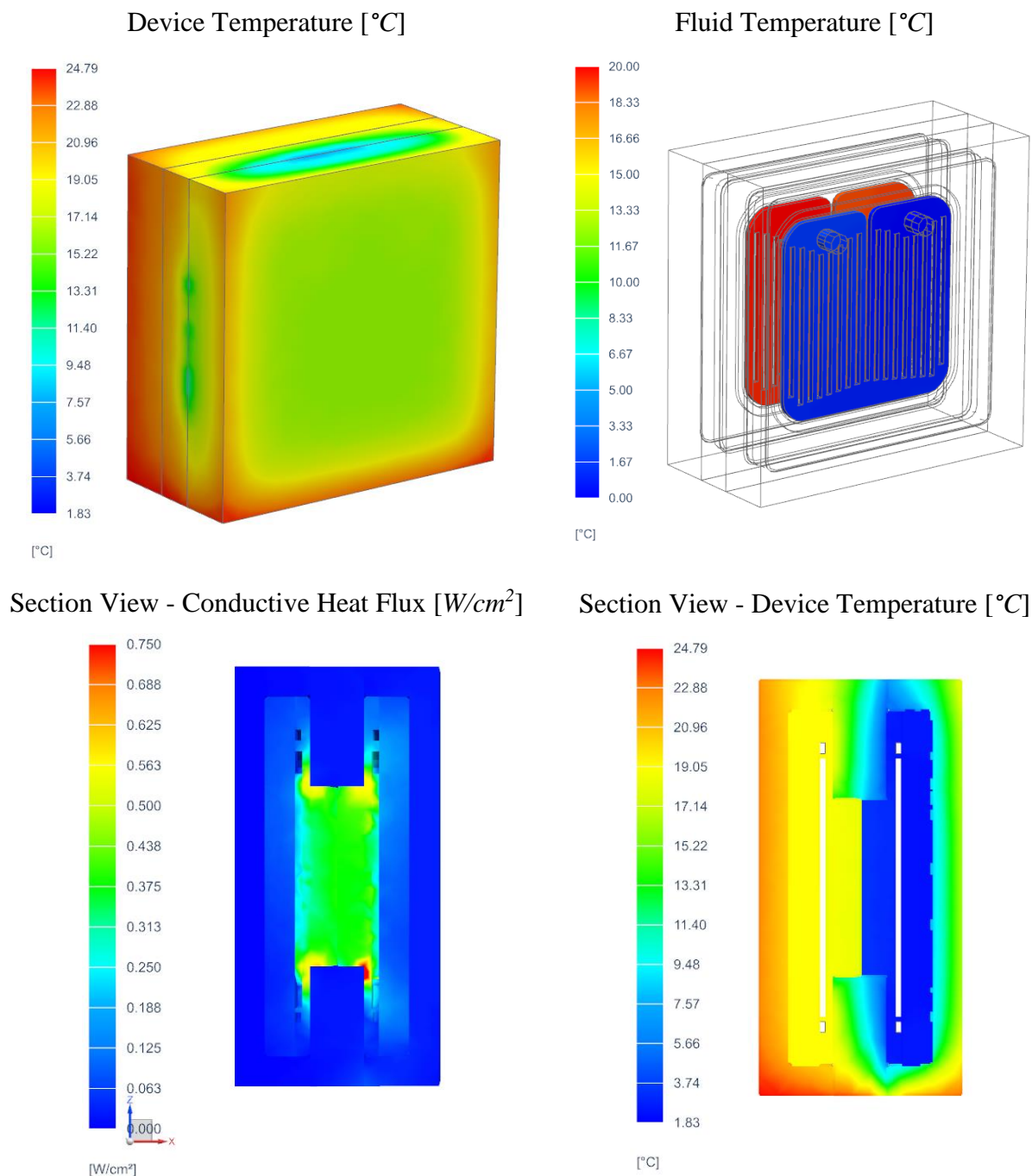
Section View - Device Temperature [℃]

Figure C.1: Example of simulation results. Shown is the device temperature (top left), fluid temperature (top right), a section view showing conductive flux (bottom left) and a section view of the device temperature (bottom right).